Lupus (2013) 22, 497–503
http://lup.sagepub.com

CONCISE REPORT

Association of a single nucleotide polymorphism in the *SH2D1A* intronic region with systemic lupus erythematosus

H Furukawa[1], A Kawasaki[2], S Oka[1], K Shimada[3,4], T Matsui[3], T Ikenaka[3], A Hashimoto[3], Y Okazaki[3], H Takaoka[3], H Futami[3], A Komiya[1], Y Kondo[5], S Ito[5,6], T Hayashi[5], I Matsumoto[5], M Kusaoi[7], Y Takasaki[7], T Nagai[8], S Hirohata[8], K Setoguchi[9], A Suda[10], S Nagaoka[10], H Kono[11], A Okamoto[12], N Chiba[13], E Suematsu[14], N Fukui[1], H Hashimoto[15], T Sumida[5], M Ono[16], N Tsuchiya[2] and S Tohma[1]

[1]Clinical Research Center for Allergy and Rheumatology, Sagamihara Hospital, National Hospital Organization, Japan; [2]Molecular and Genetic Epidemiology Laboratory, Faculty of Medicine, University of Tsukuba, Japan; [3]Department of Rheumatology, Sagamihara Hospital, National Hospital Organization, Japan; [4]Tokyo Metropolitan Tama Medical Center, Japan; [5]Division of Clinical Immunology, Faculty of Medicine, University of Tsukuba, Japan; [6]Department of Rheumatology, Niigata Rheumatic Center, Japan; [7]Division of Rheumatology, Department of Internal Medicine, Juntendo University, Japan; [8]Department of Rheumatology and Infectious Disease, Kitasato University School of Medicine, Japan; [9]Allergy and Immunological Diseases, Tokyo Metropolitan Cancer and Infectious Diseases Center Komagome Hospital, Japan; [10]Department of Rheumatology, Yokohama Minami Kyosai Hospital, Japan; [11]Department of Internal Medicine, Teikyo University, Japan; [12]Department of Rheumatology, Himeji Medical Center, National Hospital Organization, Japan; [13]Department of Rheumatology, Morioka Hospital, National Hospital Organization, Japan; [14]Department of Internal Medicine and Rheumatology, Clinical Research Institute, Kyushu Medical Center, National Hospital Organization, Japan; [15]Juntendo University School of Medicine, Japan; and [16]Department of Pathology, Tohoku University Graduate School of Medicine, Japan

SH2D1A, also known as signaling lymphocytic activation molecule (SLAM)-associated protein (SAP), is an adaptor protein. Recently, it was reported that SAP deficient mice were protected from systemic lupus erythematosus (SLE). In this study, we postulated *SH2D1A* gene to be a candidate susceptibility gene for SLE and analyzed its association with SLE. A case-control association study was conducted on 5 tag single nucleotide polymorphisms (SNPs) in *SH2D1A* region in 506 Japanese female SLE patients and 330 healthy female controls. The luciferase assay was performed to determine the functional role of the SNP associated with SLE. One SNP in the intron 2, rs2049995, showed association with SLE ($p = 0.0110$, odds ratio (OR) 1.97, 95% confidence interval (CI) 1.16–3.34, under the dominant model). The association of rs2049995 seemed to be stronger in the subset with the age of onset less than 20 years ($p = 0.0067$, OR 2.65, 95% CI 1.28–5.46). Functional evaluation of rs2049995 showed that reporter gene activity was increased 1.9-fold for the susceptible allele compared with the resistant allele. An intronic SNP of *SH2D1A* is associated with SLE. *Lupus* (2013) **22**, 497–503.

Key words: Systemic lupus erythematosus; medical genetics; single nucleotide polymorphism; SH2D1A; SLAM-associated protein

Introduction

Signaling lymphocytic activation molecule (SLAM) family receptors belong to the immunoglobulin (Ig) superfamily, possessing either two or four Ig domains in the extracellular domain of the molecule and one or more immunoreceptor tyrosine-based switching motifs (ITSM, TI/VYXXV/I) in their cytoplasmic tails, which bind to the Src homology 2 (SH2) domain of a SLAM-associated protein (SAP, SH2D1A) molecule. SAP is an adaptor molecule containing an SH2 domain and a short C-terminal tail.[1] It is expressed in T, NK and NKT cells. The binding of SAP with SLAM in T cells results in the subsequent recruitment of the Src family kinase Fyn, leading to the activation of NF-χB, resulting in IL-4 production and Th2 responses.[2] The SAP gene in humans, *SH2D1A*, is located on the X chromosome (Xq25), and in the mouse, *Sh2d1a*, it is located on the mouse XA4 chromosome region.[1]

We found spontaneous mutants in the MRL/Mp-*Fas*$^{lpr/lpr}$ (MRL/lpr) mice, a lupus-prone strain of mice. The long-living mutant MRL/Mp-*Fas*$^{lpr/lpr}$.*Sap*$^{rpl/-}$ (MRL/lpr/rpl) mice displayed minimal autoimmune phenotypes.[3] A positional cloning study revealed that there was a frameshift mutation in the *Sh2d1a* gene of the MRL/lpr/rpl mice. In addition, Fyn-deficient MRL/lpr mice lost the lupus phenotypes similar to MRL/lpr/rpl mice.[4] These findings indicated that the SLAM-SAP signaling pathway is essential for the induction of lupus.

Genetic studies using lupus-prone mice identified a lupus susceptibility locus, *Sle1b*, which overlapped with the loci of SLAM family receptors. One of these SLAM family receptor genes, *Ly108*, was shown to cause lupus.[5] A polymorphic *z* allele of *Sle1b* from the NZW strain altered the expression pattern of two splicing variants of *Ly108* and increased susceptibility to lupus. In genetic studies on systemic lupus erythematosus (SLE) patients, single nucleotide polymorphisms (SNPs) in the *LY9* gene, one of the SLAM family receptor genes, were associated with SLE susceptibility in Europeans.[6] It was also reported that SNPs in *2B4*, one of the SLAM family receptor genes, were associated with rheumatoid arthritis (RA) and with SLE in Japanese patient cohorts.[7] In addition, the expression of SAP was reduced in peripheral T cells from RA patients,[8,9] whereas the expression of SLAM was increased in peripheral B cells from these patients.[10] Thus, the SLAM-SAP signaling pathway is important for the development of lupus traits and other autoimmune diseases. In this study, we analyzed five *SH2D1A* tag SNPs in Japanese female SLE patients and healthy female controls.

Materials and methods

Patients and controls

Five hundred and six female patients with SLE (mean age ± standard deviation (SD), 44.6 ± 14.2 years) and 330 female healthy controls (mean age ± SD, 30.6 ± 8.8 years) were recruited at Sagamihara Hospital, University of Tsukuba, Juntendo University, Kitasato University, Komagome Hospital, the University of Tokyo, Himeji Medical Center, Morioka Hospital, Kyushu Medical Center and Yokohama Minami Kyosai Hospital. All patients and healthy individuals were native Japanese living in Japan. All patients with SLE fulfilled the American College of Rheumatology criteria for SLE.[11] Since *SH2D1A* is located on the X chromosome, male and female individuals should be analyzed separately. However, due to the female predominance of SLE (female to male ratio 9:1), the sample size of male SLE patients was too small to be analyzed statistically. Therefore, male patients and controls were excluded from this study.[12] This study was reviewed and approved by the research ethics committees of Sagamihara Hospital, Yokohama Minami Kyosai Hospital, Juntendo University, Kitasato University, Komagome Hospital, the University of Tokyo, Himeji Medical Center, Morioka Hospital, Kyushu Medical Center, University of Tsukuba and Tokyo Metropolitan Tama Medical Center. Written informed consent was obtained from all study participants. This study was conducted in accordance with the principles expressed in the Declaration of Helsinki.

Genotyping

Five tag SNPs in *SH2D1A* region were selected based on the HapMap Phase II JPT (Japanese) data obtained from HapMap database (http://hapmap.ncbi.nlm.nih.gov/) with the criteria of minor allele frequency >0.01 and an r^2 threshold of 0.8. Genotyping of these five tag SNPs was carried out using the cycle sequencing method with the ABI PRISM 3100 Genetic Analyzer (Applied Biosystems, Foster City, California, USA) or TaqMan genotyping assay on 7300 or 7500 Fast Real-Time polymerase chain reaction (PCR) System (Applied Biosystems), according to the manufacturer's instructions. Thermal cycling conditions consisted of initial denaturation at 95°C for 10 min, followed by 50 cycles of 95°C for 15 s followed by 60°C for 1 min. rs6608190 [T/G] was genotyped using Custom TaqMan SNP Genotyping Assays. TaqMan SNP Genotyping Assays used in this study were as follows: Assay ID: C__29241299_10 (rs7357894 [A/G]), C__11614964_10 (rs2049995[T/G]), C__16174992_10 (rs2239481 [C/T]), and C__30427796_10 (rs10284199[C/T]).

Luciferase assay

SH2D1A promoter region (−669 ~ −1) was cloned between the KpnI and XhoI restriction sites of pGL3-Basic plasmid (Promega, Madison, Wisconsin, USA) upstream of *luc* gene in the forward direction. *SH2D1A* promoter was amplified from an individual homozygous for a haplotype of −631A (rs990545[A/G]), −494G (rs7357894[A/G]), −346T (rs12164382[C/T]) and −112G (rs79572799[G/T]) using the following primers: (KSAP5U-1(+): 5'-GGTACCGTGAGGTAGAAGGAAGAGGGAGAAG-3', and XSAP5U-1(−): 5'-CTCGAGGGCCTGGTGGACTCTTGGGCAGG-3'). This vector was named pGL3-SH2D1Apro.

Correspondence to: Hiroshi Furukawa, Clinical Research Center for Allergy and Rheumatology, Sagamihara Hospital, National Hospital Organization, 18-1 Sakuradai, Minami-ku, Sagamihara 252-0392, Japan.
Email: h-furukawa@sagamihara-hosp.gr.jp
Received 30 October 2012; accepted 21 January 2013

© The Author(s), 2013. Reprints and permissions: http://www.sagepub.co.uk/journalsPermissions.nav
10.1177/0961203313479421

Subsequently, a 5' portion of the *SH2D1A* intron 2 sequence (NT_011786: 19482-20068, 587 bp) was cloned into the SalI site of pGL3-SH2D1Apro plasmid downstream of *luc* gene in the forward direction. The cloned 587 bp fragment of the *SH2D1A* intron 2 was amplified from individuals homozygous for haplotypes of 277del (rs5903659 [-/AAAG]), 317G (rs2049995[G/T]), and 392C (rs2206017[A/C]) or 277del, 317T, and 392C using the following primers: (SAPi2-1.1(+): 5'- GTATAGTTGTATTT ATTTTTGCTTCTG-3', and SAPi2-6.4(−): 5'-ATAAGGGAGGATTCTTAGGC-3'). The two vectors were named pGL3-SH2D1Apro-G and pGL3-SH2D1Apro-T based on the polymorphism in 317 (rs2049995, Figure 1(B)). One hundred thousand Jurkat lymphoma cells (provided by Tohoku University, Institute of Development, Aging and Cancer, Cell Resource Center for Biomedical Research) were cotransfected with 20 ng pRL-TK Vector (Promega) and 180 ng of pGL3-SH2D1Apro, pGL3-SH2D1Apro-G or pGL3-SH2D1Apro-T vector using 0.6 µl of Transfectin™ (Bio-rad, Hercules, California, USA). Luciferase assay was performed after 48 h with Dual-Luciferase Reporter Assay System (Promega), according to the manufacturer's instruction. Data are shown as relative luciferase activity (Firefly/Renilla).

Analysis of gene expression by real-time quantitative PCR

RNA was extracted from peripheral blood mononuclear cells (PBMCs) and complementary DNA

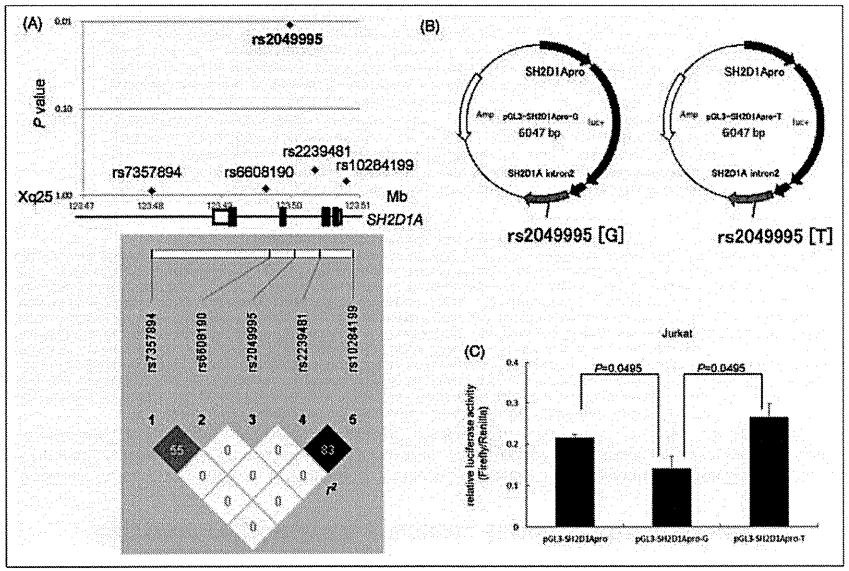

Figure 1 (A) Association study of five single nucleotide polymorphisms (SNPs) in *SH2D1A* gene with systemic lupus erythematosus (SLE). In the upper panel, *p* values under the dominant model for minor alleles are indicated. Association was tested by chi-square analysis using 2 × 2 contingency tables. In the lower panel, r^2 values based on data from 330 female healthy individuals are shown. (B) The two constructs, pGL3-SH2D1Apro-G and pGL3-SH2D1Apro-T (containing a portion of intron 2 of SH2D1A gene with SNP rs2049995[T/G]), used in the luciferase assay. (C) Relative luciferase activity in Jurkat cells cotransfected with pGL3-SH2D1Apro, pGL3-SH2D1Apro-G or pGL3-SH2D1Apro-T vector and the internal control pRL-TK vector. Relative luciferase activity was normalized to Renilla luciferase activity of the internal control. The experiments were performed in triplicate and the mean value with standard deviation is shown. Mann–Whitney U test was performed in the comparison of luciferase assay results. The data shown are representative of three independent experiments.

(cDNA) was synthesized using Superscript III reverse transcriptase (Invitrogen, Carlsbad, California, USA). Gene expression was evaluated quantitatively by real-time PCR using a TaqMan Gene Expression Assay on 7500 Fast Real-Time PCR System. Thermal cycling conditions consisted of initial denaturation at 95°C for 20 s, followed by 40 cycles of 95°C for 3 s followed by 60°C for 30 s. The amount of specific cDNA was quantified using comparative Threshold Cycle (CT) method. The levels of cDNA among samples were normalized to the expression of *GAPDH*. The TaqMan Gene Expression Assay used in this study was Hs00158978_m1 for *SH2D1A*.

Statistical analysis

Differences in allele and genotype frequencies between SLE patients and healthy controls were analyzed by chi-square test using 2 × 2 contingency tables. When one or more of the variables in the contingency tables were 5 or less, Fisher's exact test was employed. Linkage disequilibrium (LD) was analyzed using Haploview v4.2 (Broad Institute, Cambridge, Massachusetts, USA). Pairwise r^2 values were calculated based on the genotypes of 330 healthy controls. The Mann–Whitney U test was performed in the comparison of luciferase assay and real-time quantitative PCR results.

Results

Associations of an SNP in SH2D1A with SLE

Five tag SNPs in *SH2D1A* gene were analyzed in Japanese female SLE patients and healthy female controls. No deviation from Hardy-Weinberg equilibrium was observed in the patients and the controls ($p > 0.05$). There are three LD blocks including the five SNPs examined in this study (Figure 1(A)) and the adjustment for multiple comparisons using the Bonferroni method defined statistical significance as $p < 0.0167$ for this study. A significant association was observed for one SNP in intron 2, rs2049995 ($p = 0.0110$, odds ratio (OR) 1.97, 95% confidence interval (CI) 1.16–3.34, under the dominant model for the minor allele, Table 1, Figure 1(A)). Thus, an intronic SNP of *SH2D1A* is associated with SLE.

Associations of rs2049995 with clinical subsets of SLE

We determined whether rs2049995 SNP was associated with clinical phenotypes (Table 2).

Table 1 Association of *SH2D1A* single nucleotide polymorphisms (SNPs) with systemic lupus erythematosus (SLE)

					Allelic association			*Dominant model*			*Recessive model*		
	Genotype			*Allele frequency*	p	*OR*	*(95% CI)*	p	*OR*	*(95% CI)*	p	*OR*	*(95% CI)*
rs7357894	A/A	G/A	G/G	A									
SLE	30 (5.9)	167 (33.0)	309 (61.1)	227 (22.4)	0.8246	1.03	(0.81–1.30)	0.8966	1.02	(0.77–1.35)	0.7732	1.09	(0.60–1.99)
Controls	18 (5.5)	109 (33.0)	203 (61.5)	145 (22.0)									
rs6608190	T/T	G/T	G/G	T									
SLE	36 (7.1)	185 (36.6)	285 (56.3)	257 (25.4)	0.9108	1.01	(0.81–1.27)	0.8540	1.03	(0.78–1.36)	0.9310	0.98	(0.57–1.67)
Controls	24 (7.3)	118 (35.8)	188 (57.0)	166 (25.2)									
rs2049995	T/T	G/T	G/G	T									
SLE	0 (0.0)	57 (11.3)	449 (88.7)	57 (5.6)	0.0202	1.82	(1.09–3.03)	0.0110	1.97	(1.16–3.34)	0.3947 [a]	0.22	(0.01–5.34)
Controls	1 (0.3)	19 (5.8)	310 (93.9)	21 (3.2)									
rs2239481	C/C	T/C	T/T	C									
SLE	56 (11.1)	221 (43.7)	229 (45.3)	333 (32.9)	0.4300	1.09	(0.88–1.34)	0.5109	1.10	(0.83–1.45)	0.5280	1.16	(0.73–1.83)
Controls	32 (9.7)	141 (42.7)	157 (47.6)	205 (31.1)									
rs10284199	C/C	T/C	T/T	C									
SLE	56 (11.1)	227 (44.9)	223 (44.1)	339 (33.5)	0.6953	1.04	(0.85–1.28)	0.6941	1.06	(0.80–1.40)	0.8343	1.05	(0.67–1.64)
Controls	35 (10.6)	145 (43.9)	150 (45.5)	215 (32.6)									

CI: confidence interval; OR: odds ratio.
Genotype and allele frequency are shown in parenthesis (%). Association was tested by chi-square analysis or Fisher's exact test using 2 × 2 contingency tables under the indicated models for minor alleles.
[a]Fisher's exact test was employed.

Association of this SNP with each phenotype of SLE was tested. A significant association was found for rs2049995 in the subset with the age of onset less than 20 years ($p = 0.0067$, OR 2.65, 95% CI 1.28–5.46, Table 2), arthritis ($p = 0.0028$, OR 2.40, 95% CI 1.33–4.33), or lymphopenia ($p = 0.0017$, OR 2.47, 95% CI 1.39–4.42). The association of rs2049995 with anti-dsDNA ($p = 0.0094$, OR 2.05, 95% CI 1.18–3.54), anti-Ro/SSA ($p = 0.0087$, OR 2.35, 95% CI 1.22–4.51), or anti-La/SSB ($p = 0.0118$, OR 3.62, 95% CI 1.41–9.25) antibodies remained significant. Thus, rs2049995 SNP was associated with clinical subsets of SLE.

The effect of rs2049995 SNP on luciferase activity in Jurkat cells

The effect of rs2049995 SNP on the expression of *SH2D1A* was evaluated by luciferase assay. A 587 bp fragment of the 5'- portion of the *SH2D1A* intron 2 was cloned downstream of *SH2D1A* promoter and *luc* in the pGL3 vector (Figure 1(B)) and the luciferase activity was analyzed in Jurkat cells transfected with the vectors. The vector containing susceptible allele [T] of rs2049995 showed a 1.9-fold increase in luciferase activity compared with that containing the resistant allele [G] ($p = 0.0495$, by Mann–Whitney U test, Figure 1(C)). Two additional experiments were performed and resulted in the similar conclusion ([T]/[G] luciferase activity ratio = 1.9, 2.0; $p = 0.0495$, 0.0495, respectively). Thus, functional evaluation of rs2049995 showed increased reporter gene activity in the susceptible allele.

The effect of rs2049995 SNP on SH2D1A gene expression in PBMCs

Association between rs2049995 SNP and *SH2D1A* mRNA levels was tested by use of the Mann–Whitney U test (Supplementary Figure 1). Difference of gene expression levels was not observed between two genotypes, G/G and G/T, in healthy controls or SLE patients because of the small sample number of individuals with G/T genotype or the immunosuppressive treatment for SLE.

Discussion

Recent studies have shown that the SLAM-SAP signaling pathway contributes to the susceptibility to autoimmune diseases. Since SAP-deficient mice

Table 2 Association of rs2049995 with clinical characteristics of systemic lupus erythematosus (SLE)

	Phenotype	*Genotype*			*Allele frequency*		*Allelic association*			*Dominant model*		
		T/T	G/T	G/G	T	G	p	*OR*	*(95% CI)*	p	*OR*	*(95% CI)*
rs2049995												
Controls		1 (0.3)	19 (5.8)	310 (93.9)	21 (3.2)	639 (96.8)						
Age of onset <20	96 (20.0)	0 (0.0)	14 (14.6)	82 (85.4)	14 (7.3)	178 (92.7)	0.0116	2.39	(1.19–4.80)	0.0067	2.65	(1.28–5.46)
Malar rash (+)	173 (34.2)	0 (0.0)	19 (11.0)	154 (89.0)	19 (5.5)	327 (94.5)	0.0749	1.77	(0.94–3.34)	0.0499	1.91	(0.99–3.69)
Photosensitivity (+)	152 (30.0)	0 (0.0)	17 (11.2)	135 (88.8)	17 (5.6)	287 (94.4)	0.0739	1.80	(0.94–3.47)	0.0496	1.95	(0.99–3.84)
Arthritis (+)	231 (45.7)	0 (0.0)	31 (13.4)	200 (86.6)	31 (6.7)	431 (93.3)	0.0057	2.19	(1.24–3.86)	0.0028	2.40	(1.33–4.33)
Serositis (+)	76 (16.4)	0 (0.0)	10 (13.2)	66 (86.8)	10 (6.6)	142 (93.4)	0.0488	2.14	(0.99–4.65)	0.0330	2.35	(1.05–5.25)
Renal disorder (+)	238 (49.3)	0 (0.0)	22 (9.2)	216 (90.8)	22 (4.6)	454 (95.4)	0.2095	1.47	(0.80–2.71)	0.1526	1.58	(0.84–2.96)
Neurologic disorder (+)	102 (21.7)	0 (0.0)	11 (10.8)	91 (89.2)	11 (5.4)	193 (94.6)	0.1440	1.73	(0.82–3.66)	0.1062	1.87	(0.87–4.05)
Lymphopenia (+)	247 (48.8)	0 (0.0)	34 (13.8)	213 (86.2)	34 (6.9)	460 (93.1)	0.0035	2.25	(1.29–3.93)	0.0017	2.47	(1.39–4.42)
Anti-dsDNA Abs (+)	386 (82.1)	0 (0.0)	45 (11.7)	341 (88.3)	45 (5.8)	727 (94.2)	0.0172	1.88	(1.11–3.20)	0.0094	2.05	(1.18–3.54)
Anti-Sm Abs (+)	116 (25.2)	0 (0.0)	13 (11.2)	103 (88.8)	13 (5.6)	219 (94.4)	0.0975	1.81	(0.89–3.67)	0.0685	1.96	(0.94–4.07)
Anti-RNP Abs (+)	115 (22.7)	0 (0.0)	14 (12.2)	101 (87.8)	14 (6.1)	216 (93.9)	0.0509	1.97	(0.99–3.95)	0.0336	2.15	(1.05–4.41)
Anti-Ro/SSA Abs (+)	152 (30.0)	0 (0.0)	20 (13.2)	132 (86.8)	20 (6.6)	284 (93.4)	0.0152	2.14	(1.14–4.02)	0.0087	2.35	(1.22–4.51)
Anti-La/SSB Abs (+)	37 (7.3)	0 (0.0)	7 (18.9)	30 (81.1)	7 (9.5)	67 (90.5)	0.0166[a]	3.18	(1.30–7.75)	0.0118[a]	3.62	(1.41–9.25)

Abs: antibodies; CI: confidence interval; dsDNA: double-strand DNA; OR: odds ratio; RNP: ribonucleoprotein.
Phenotype, genotype and allele frequency are shown in parenthesis (%). Association was tested by chi-square analysis or Fisher's exact test using 2 × 2 contingency tables under the indicated models for rs2049995T allele. Each SLE subset of clinical characteristics was compared with healthy controls.
[a]Fisher's exact test was employed.

were protected from lupus traits,[3] we postulated that *SH2D1A* polymorphisms might also contribute to SLE. To investigate the possibility, we analyzed five tag SNPs in *SH2D1A* and found associations of one SNP with SLE. To our knowledge, this is the first report of such associations with SLE. Our findings suggest a role for the SLAM-SAP signaling pathway in the pathogenesis of human autoimmune disease as well as autoimmune mouse models.

The association of the polymorphisms in *SH2D1A* and SLE was not reported even in genome wide association studies. It was suggested that the allele frequency of rs2049995 SNP is not high enough to be found in genome wide association study. In addition, the X chromosome was not analyzed in genome wide association studies.[13–15] We cannot rule out the possibility that other causative SNPs tagged by rs2049995 might exist. This possibility could be addressed by resequencing the entire *SH2D1A* region. As a result of the limited sample size of this study, the observed statistical association was modest. The associations of the SNP should be confirmed in future independent studies. Since the allele frequencies of rs2049995 SNP in other ethnic populations are higher than that in Japanese (0.034 in HapMap-JPT (Japanese), 0.108 in HapMap-CEU (European), 0.078 in HapMap-HCB (Chinese), and 0.292 in HapMap-YRI (Yoruba); data obtained from HapMap database), the role of rs2049995 SNP for SLE in other populations should be determined. In future studies, gel shift assays should be done on the SNP rs2049995 to identify the molecules involved in the regulation of *SH2D1A* expression.

Furthermore, the luciferase assay revealed the augmented reporter gene activity in the susceptible allele of rs2049995. Higher *SH2D1A* gene expression levels caused by the susceptible [T] allele of rs2049995 might effectively transduce signals in the SLAM-SAP signaling pathway of T cells, which would develop SLE. However, association of the intronic SNP with levels of *SH2D1A* mRNA was not actually confirmed. The mRNA levels should be examined in T or NK cells from a considerable number of healthy controls or SLE patients before starting immunosuppressive treatment, because SAP molecules were mainly expressed in T and NK cells.

This is the first identification of associations of an intronic SNP in *SH2D1A* with SLE. Our findings support the crucial role of SLAM-SAP signaling pathway in SLE pathogenesis.

Funding

This work was supported by Grants-in-Aid for Scientific Research (B, C) (22390199, 22591090) from the Japan Society for the Promotion of Science, Health and Labour Science Research Grants from the Ministry of Health, Labour, and Welfare of Japan, Grants-in-Aid for Clinical Research from the National Hospital Organization, research grants from Daiwa Securities Health Foundation, Japan Research Foundation for Clinical Pharmacology, The Nakatomi Foundation, Takeda Science Foundation and from pharmaceutical companies: Abbott Japan Co., Ltd, Astellas Pharma Inc., Chugai Pharmaceutical Co., Ltd, Eisai Co., Ltd, Mitsubishi Tanabe Pharma Corporation, Merck Sharp and Dohme Inc., Pfizer Japan Inc., Takeda Pharmaceutical Company Ltd, Teijin Pharma Ltd. The funders had no role in study design, data collection and analysis, decision to publish or preparing the manuscript.

Conflicts of interest

HF has the following conflicts and the following funders are supported in whole or in part by the indicated pharmaceutical companies. The Japan Research Foundation for Clinical Pharmacology is run by Daiichi Sankyo, the Takeda Science Foundation is supported by an endowment from Takeda Pharmaceutical Company and the Nakatomi Foundation was established by Hisamitsu Pharmaceutical Co., Inc. The Daiwa Securities Health Foundation was established by Daiwa Securities Group Inc.

ST was supported by research grants from nine pharmaceutical companies: Abbott Japan Co., Ltd, Astellas Pharma Inc., Chugai Pharmaceutical Co., Ltd, Eisai Co., Ltd, Mitsubishi Tanabe Pharma Corporation, Merck Sharp and Dohme Inc., Pfizer Japan Inc., Takeda Pharmaceutical Company Ltd and Teijin Pharma Ltd.

NT is supported by the Takeda Science Foundation which is supported by an endowment from Takeda Pharmaceutical Company.

The other authors declare no financial or commercial conflict of interest.

Acknowledgements

The authors would like to thank Mayumi Yokoyama (Sagamihara Hospital) for secretarial

assistance. M Ono, N Tsuchiya, and S Tohma contributed equally to this work.

References

1 Furukawa H, Tohma S, Kitazawa H, Komori H, Nose M, Ono M. Role of SLAM-associated protein in the pathogenesis of autoimmune diseases and immunological disorders. *Arch Immunol Ther Exp* 2010; 58: 37–44.
2 Veillette A. Immune regulation by SLAM family receptors and SAP-related adaptors. *Nat Rev Immunol* 2006; 6: 56–66.
3 Komori H, Furukawa H, Mori S, *et al.* A signal adaptor SLAM-associated protein regulates spontaneous autoimmunity and Fas-dependent lymphoproliferation in MRL-Faslpr lupus mice. *J Immunol* 2006; 176: 395–400.
4 Takahashi T, Yagi T, Kakinuma S, *et al.* Suppression of autoimmune disease and of massive lymphadenopathy in MRL/Mp-lpr/lpr mice lacking tyrosine kinase Fyn (p59fyn). *J Immunol* 1997; 159: 2532–2541.
5 Kumar K, Li L, Yan M, *et al.* Regulation of B cell tolerance by the lupus susceptibility gene Ly108. *Science* 2006; 312: 1665–1669.
6 Cunninghame GDS, Vyse TJ, Fortin PR, *et al.* Association of LY9 in UK and Canadian SLE families. *Genes Immun* 2008; 9: 93–102.
7 Suzuki A, Yamada R, Kochi Y, *et al.* Functional SNPs in CD244 increase the risk of rheumatoid arthritis in a Japanese population. *Nat Genet* 2008; 40: 1224–1229.
8 Takei M, Ishiwata T, Mitamura K, *et al.* Decreased expression of signaling lymphocytic-activation molecule-associated protein (SAP) transcripts in T cells from patients with rheumatoid arthritis. *Int Immunol* 2001; 13: 559–565.
9 Sawada S, Takei M. Epstein-Barr virus etiology in rheumatoid synovitis. *Autoimmun Rev* 2005; 4: 106–110.
10 Isomaki P, Aversa G, Cocks B, *et al.* Increased expression of signaling lymphocytic activation molecule in patients with rheumatoid arthritis and its role in the regulation of cytokine production in rheumatoid synovium. *J Immunol* 1997; 159: 2986–2993.
11 Hochberg M. Updating the American College of Rheumatology revised criteria for the classification of systemic lupus erythematosus. *Arthritis Rheum* 1997; 40: 1725–1725.
12 Kawasaki A, Furukawa H, Kondo Y, *et al.* TLR7 single-nucleotide polymorphisms in the 3' untranslated region and intron 2 independently contribute to systemic lupus erythematosus in Japanese women: A case-control association study. *Arthritis Res Ther* 2011; 13: R41.
13 Han JW, Zheng HF, Cui Y, *et al.* Genome-wide association study in a Chinese Han population identifies nine new susceptibility loci for systemic lupus erythematosus. *Nat Genet* 2009; 41: 1234–1237.
14 Harley JB, Alarcon-Riquelme ME, Criswell LA, *et al.* Genome-wide association scan in women with systemic lupus erythematosus identifies susceptibility variants in ITGAM, PXK, KIAA1542 and other loci. *Nat Genet* 2008; 40: 204–210.
15 Okada Y, Shimane K, Kochi Y, *et al.* A genome-wide association study identified AFF1 as a susceptibility locus for systemic lupus eyrthematosus in Japanese. *PLoS Genet* 2012; 8: e1002455.

http://dx.doi.org/10.7567/JJAP.52.04CL03

Fabrication and In vivo Evaluation of Poly(3,4-ethylenedioxythiophene) Stimulus Electrodes for Fully Implantable Retinal Prosthesis

Chikashi Kigure[1], Hideki Naganuma[2], Yuichiro Sasaki[1], Hisashi Kino[2], Hiroshi Tomita[3], and Tetsu Tanaka[1,2*]

[1]*Department of Biomedical Engineering, Graduate School of Biomedical Engineering, Tohoku University, Sendai 980-8579, Japan*
[2]*Department of Bioengineering and Robotics, Graduate School of Engineering, Tohoku University, Sendai 980-8579, Japan*
[3]*Department of Chemistry and Bioengineering, Faculty of Engineering, Iwate University, Morioka 020-8551, Japan*
E-mail: link@lbc.mech.tohoku.ac.jp

Received September 23, 2012; revised December 18, 2012; accepted December 20, 2012; published online April 22, 2013

The development of poly(3,4-ethylenedioxythiophene) (PEDOT) stimulus electrodes and the relationship between the electrical stimulation of a rabbit retina and electrically evoked potential (EEP) were studied in detail. We fabricated implantable flexible cables with Pt, IrO_x, and PEDOT electrodes and evaluated the electrochemical impedances (EIs) and charge injection capacities (CICs) of such electrodes. From the result, we confirmed that PEDOT electrodes have both lower EIs and larger CICs than Pt and IrO_x electrodes. In addition, we performed in vivo experiments with PEDOT electrodes and clarified the relationships between the electrical stimulation of the rabbit retina and EEP. It is highly probable that visual restoration will be realized safely with PEDOT electrodes. © 2013 The Japan Society of Applied Physics

1. Introduction

Recently, many studies of retinal prostheses for restoring visual sensation in blind patients by the electrical stimulation of the remaining retinal cells using stimulus electrodes have been reported.[1,2] Clinical trials of retinal prostheses have been vigorously conducted in several research institutes around the world.[3–7] We have been developing a fully implantable retinal prosthesis with a three-dimensional (3D) stacked retinal prosthesis chip (Fig. 1) to achieve a small high-resolution artificial retina that will restore high quality of life (QOL) in blind patients.[8] In order to realize visual restoration with high resolution, it is necessary to increase the number of stimulus electrodes and to miniaturize stimulus electrodes. As the size of stimulus electrodes decreases, their electrochemical impedance (EI) increases and their injection charge decreases in amount. These phenomena are avoided in stimulating retinal cells safely. Therefore, it is necessary to use small stimulus electrodes having both lower EIs and larger charge injection capacities (CICs).

In this study, we fabricated stimulus electrodes with three materials, namely, Pt, IrO_x, and poly(3,4-ethylenedioxythiophene) (PEDOT) on implantable flexible cables, and evaluated their EIs and CICs from the viewpoint of retinal stimulus electrodes. PEDOT is a conductive polymer with a small charge transfer resistance and a large electric double layer awing to its large reactive area. Therefore, lower impedance magnitudes and larger CIC are expected even when small PEDOT electrodes are used as stimulus electrodes. We fabricated Pt and IrO_x electrodes for comparison because they were mentioned in other studies of retinal prosthesis. We performed in vivo experiments with the stimulus electrodes using a rabbit. We electrically stimulated the retina with the stimulus electrodes implanted in the rabbit eyeball and measured electrically evoked potential (EEP) from the visual cortex of the rabbit. Although many research organizations have performed animal experiments, the relationships between parameters of the electrical stimulation and EEP have not been clarified yet.[9–12] We measured EEP with PEDOT electrodes under various stimulus conditions and performed qualitative investigations of the rabbit.

2. Fabrication of Pt, IrO_x, and PEDOT Electrodes on Flexible Cables

We fabricated flexible cables with stimulus electrode arrays using conventional semiconductor processing technology. Figure 2 shows the process flow of the fabrication of flexible cables. First, SiO_2 was deposited on a Si substrate as the sacrificial layer. A photosensitive coating material (PCM) was spin-coated and cured at 350 °C. The PCM used in this study is an insulating resin suitable for use in vivo because the PCM has a very low water absorption percentage of approximately 0.9%. The PCM layer formed had a thickness of approximately 3 μm. Either a Pt or Ir electrode was formed by a conventional lift-off process. Pt was also used as the base material of PEDOT electrodes, and Ir was used to form IrO_x electrodes. Then, a thick polyimide layer was spin-coated and cured at 350 °C. The polyimide layer was 15 μm thick. Both Au and Cr wirings were formed by sputtering and etching. These metal wirings were then covered with a PCM layer. Finally, the Si substrate was dipped in a buffered HF solution to peel off a flexible cable with stimulus electrodes. We formed IrO_x electrodes by applying square wave voltages ranging from −0.6 to 0.85 V with respect to the reference electrode to Ir electrodes immersed in phosphate-buffered saline (PBS). We also formed the PEDOT electrodes by growing a 3,4-etylenedioxythiophene (EDOT) layer on Pt electrodes using electrochemical polymerization. The electrochemical polymerization of EDOT was carried out by applying a direct current to a Pt electrode immersed in EDOT monomer solution, prepared by mixing poly(sodium-4-styrenesulfonate) and EDOT in deionized water. Figure 3 shows the fabricated flexible cable with a 10 × 10 stimulus electrode array where each electrode has a diameter of 90 μm. Enlarged photographs of Pt, IrO_x, and PEDOT electrodes are also shown in Fig. 3.

3. Experimental Results and Discussion

3.1 EI and CIC measurements of Pt, IrO_x, and PEDOT electrodes

CIC means the maximum injectable charge density that keeps an electrode potential within a potential window.

 © 2013 The Japan Society of Applied Physics

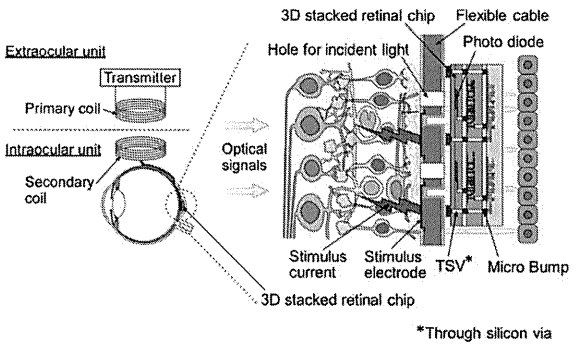

Fig. 1. (Color online) Configuration of fully implantable retinal prosthesis with 3D stacked retinal prosthesis chip.

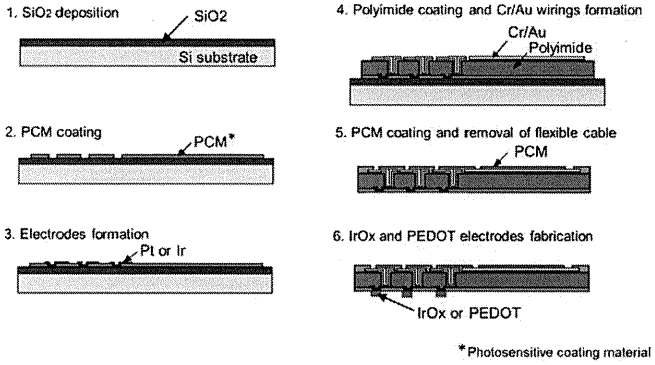

Fig. 2. (Color online) Process flow of fabrication of stimulus electrode on the flexible cable.

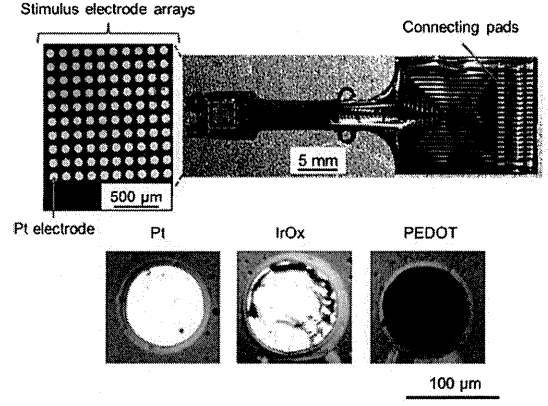

Fig. 3. (Color online) Photographs of fabricated flexible cable and Pt, IrO_x, and PEDOT electrodes.

 © 2013 The Japan Society of Applied Physics

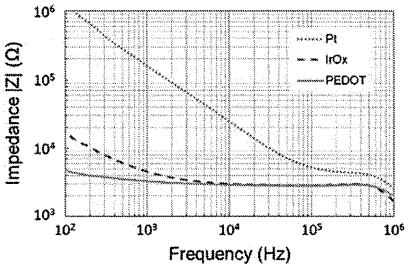

Fig. 4. (Color online) Comparison of impedance spectra of Pt, IrO_x, and PEDOT electrodes.

Table I. Comparison of CICs (mC/cm^2) of Pt, IrO_x, and PEDOT electrodes.

Material	CIC
Pt	0.11
IrO_x	0.23
PEDOT	4.03

Electrical stimulation with charge injections beyond the CIC causes an irreversible reaction at the surface of an electrode material, which leads to the corrosion of the electrode and damage to the surrounding tissues.[13] In the EI and CIC measurements, we used the Pt electrode as the counter electrode and the Ag/AgCl electrode as the reference electrode. These measurements were performed using PBS (Sigma-Aldrich D8537) at room temperature. We used a conventional CIC measurement system[13] and measured CIC with cathodic-to-anodic pulses where both cathodic and anodic pulses had widths of 0.2 ms.

Figure 4 shows the EI behaviors for different electrode materials. Conventional retinal stimulation with biphasic current pulses uses stimulus frequencies between several tens of Hz to several hundreds of Hz.[14,15] We also used stimulus frequencies between 40 to 300 Hz in this study. Although these biphasic current pulses include high-frequency elements, the biphasic currents with fundamental stimulus pulse frequencies mentioned above are most effective for retinal stimulation. The impedance magnitudes of the IrO_x and PEDOT electrodes were significantly lower than that of the Pt electrode at these frequencies, indicating that the retina can be stimulated with lower voltages using the IrO_x and PEDOT electrodes. Table I shows a summary of the CICs of the Pt, IrO_x, and PEDOT electrodes. The potential windows of the stimulus electrodes were −0.6 to 0.8 V for Pt, −0.6 to 0.8 V for IrO_x, and −0.9 to 0.9 V for PEDOT.[16] It is clearly demonstrated that the PEDOT electrode can supply thirty times larger electrical charges than the Pt and IrO_x electrodes via single stimulation. Considering these results, PEDOT can be regarded as one of the most suitable materials for retinal stimulation.

Table II shows a comparison of stimulus electrodes characteristics for retinal prostheses. The CIC of the TiN electrode measured with 200 μs was 0.87 mC/cm^2.[17] As shown in this table, among other electrodes our electrode has the largest CIC, in spite of its small electrode size.

Table II. Features of stimulus electrodes for retinal prostheses.

Institute	Object	Electrode size (μm)	Material	Reference
Second Sight	Human	ϕ300	Pt	5
Osaka Univ.	Human	ϕ500	Pt	4
Melbourne Univ.	Cat	ϕ160	Pt	11
Boston Health Care	Pig	ϕ400	IrO_x	9
Philipps Univ.	Human	ϕ100	IrO_x	6
Retina Implant	Human	50 × 50	TiN	3
This work	Rabbit	ϕ90	PEDOT	—

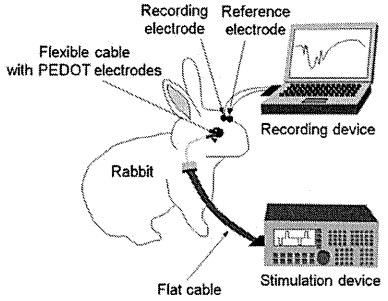

Fig. 5. (Color online) Configuration of in vivo experiment.

3.2 In vivo evaluation of PEDOT stimulus electrodes

In vivo experiments were performed using the PEDOT stimulus electrodes to investigate whether the electrodes can elicit potentials in the visual cortex. Figure 5 shows the setup of the in vivo experiments, where we used Japanese white rabbits (2–3 kg) with normal eyeballs and the PEDOT stimulus electrodes implanted inside the photoreceptor cell layer of the rabbit eyeball. We ensured that all the procedures used adhered to the Association for Research in Vision and Ophthalmology (ARVO) resolution on the use of animals in research. Figure 6 shows a photograph of the fundus of the eyeball with a stimulus electrode array implanted on a flexible cable. A recording electrode and a reference electrode were implanted in the rabbit brain. Subretinal stimulation to the retina was adopted and EEP was measured from the visual cortex of the rabbit brain. In this experiment, a cathodic stimulus current pulse with an amplitude of 600 μA and a duration of 3 ms at a time of 0 s was applied. Although the stimulus charge may exceed the CIC under certain conditions, it is appropriate to use those stimulus current pulses in order to obtain definite EEPs. For comparison, visually evoked potential (VEP) was also measured when the rabbit retina was stimulated with a light pulse at a time of 0 s. VEPs are reactions in the visual cortex elicited by optical stimulation to the retina. The light intensity was 1000 lx with a duration of 10 ms.

 © 2013 The Japan Society of Applied Physics

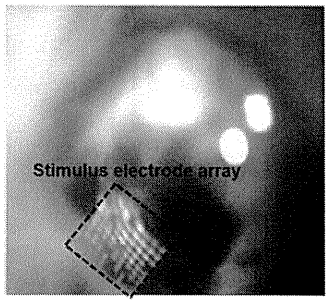

Fig. 6. (Color online) Photograph of fundus of eyeball with stimulus electrode array implanted on flexible cable.

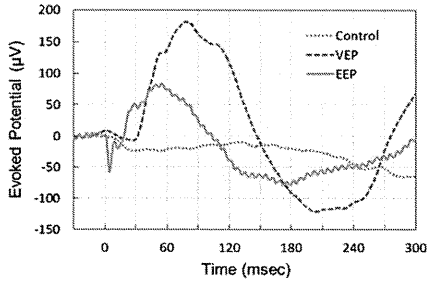

Fig. 7. (Color online) Comparison of VEP, EEP, and control waveforms measured from visual cortex of rabbit.

Figure 7 shows a comparison of waveforms under the VEP, EEP, and control conditions. The control waveform was measured without optical/electrical stimulation. All the waveforms were averages of 50 measurements. To observe changes in the brain responses caused by the presence or absence of stimulation, we used EEP without stimulation as the control. All the measurements were carried out in a completely dark room. As the pulse width of the stimulus current was 3 ms, the first negative spike in EEP was an artifact due to the cathodic stimulus current pulse. The response peak observed at 50 ms was the nerve response. In the comparison between EEP and VEP, EEP had similar response behaviors to VEP, unlike in the control condition. The EEP in Fig. 7 had similar latency and response characteristics to the EEP of other research institutions.[18,19] Therefore, we can successfully stimulate the rabbit retina by electrical stimulation with PEDOT electrodes.

In addition, other in vivo experiments were performed in order to examine the relationships between electrical stimulation and EEP in detail. In this EEP measurement, several kinds of cathodic pulses were applied to obtain fundamental information on the electrical stimulation of the retina. Pulse durations of 1, 3, and 5 ms were used with different pulse amplitudes. Figure 8 shows the relationships between the amplitude of stimulus current and the amplitude of measured EEP. Each measurement point is an average of 50 measurements. No EEPs were measured with a pulse duration of 1 ms. A moving average was plotted to briefly observe the data tendency. The moving average was calculated by taking the average of two neighboring points. Although it is difficult to determine the relationships between EEP amplitude and the stimulus current parameters awing to the small experimental population and the large variation, EEP amplitude tends to increase with an increase in stimulus current. It also tends to increase with an increase in the pulse duration of the stimulus current. It was found that EEP depends on both the amplitude and pulse duration of the stimulus current, as in previous experimental results obtained with other electrode materials. The in vivo experiments qualitatively demonstrated that the amplitude of EEP can be controlled by changing the amplitude and pulse duration of the stimulation current, which means that visual sensations can be safely restored with PEDOT stimulus electrodes.

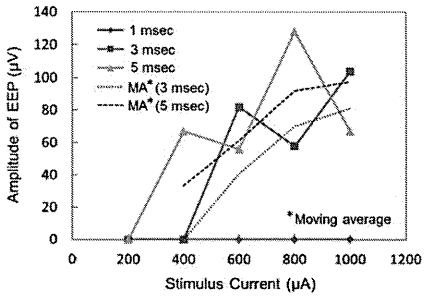

Fig. 8. (Color online) Relationships between amplitude of stimulus current and the amplitude of EEP.

4. Conclusions

Stimulus electrodes made of materials such as Pt, IrO_x, and PEDOT were fabricated on flexible cables. Their EIs and CICs were also evaluated in detail. Among the electrodes studied, the PEDOT stimulus electrodes showed the best characteristics such as the lowest EI and the largest CIC. In this study, we did not evaluate the toxicity of the PEDOT electrodes owing to acute experiments. However, the high biocompatibility of PEDOT electrodes has been reported by a different research group.[20] In in vivo experiments, neuronal reactions were successfully elicited in the visual cortex of the rabbit by electrical stimulation to the retina. Furthermore, the amplitude of measured EEP depended on both the amplitude and pulse duration of the stimulus current. It is possible to obtain EEP similarly to VEP by adjusting the amplitude and pulse duration of the stimulus current, leading to high probabilities of safe visual restoration with PEDOT stimulus electrodes.

 © 2013 The Japan Society of Applied Physics

Acknowledgements

This work was supported by the Japan Society for the Promotion of Science (JSPS) through a Grant-in-Aid for Scientific Research (A) No. 22246045. The work is also supported by the VLSI Design and Education Center (VDEC), The University of Tokyo, in collaboration with Cadence Design Systems. The devices used in this work were fabricated at the Micro/Nano-machining Research and Education Center, Tohoku University.

1) J. D. Weiland, A. K. Cho, and M. S. Humayun: Ophthalmology **118** (2011) 2227.
2) J. M. Ong and L. D. Cruz: Clin. Exp. Ophthalmol. **40** (2012) 6.
3) E. Zrenner, K. U. Bartz-Schmidt, H. Benav, D. Besch, A. Bruckmann, V. P. Gabel, F. Gekeler, U. Greppmaier, A. Harscher, S. Kibbel, J. Koch, A. Kusnyerik, T. Peters, K. Stingl, H. Sachs, A. Stett, P. Szurman, B. Wilhelm, and R. Wilke: Proc. R. Soc. B **278** (2011) 1489.
4) T. Fujikado, M. Kamei, H. Sakaguchi, H. Kanda, T. Morimoto, Y. Ikuno, K. Nishida, H. Kishima, T. Maruo, K. Konoma, M. Ozawa, and K. Nishida: Invest. Ophthalmol. Visual Sci. **52** (2011) 4726.
5) M. S. Humayun, J. D. Dorn, L. D. Cruz, G. Dagnelie, J. Sahel, P. E. Stanga, A. V. Cideciyan, J. L. Duncan, D. Eliott, E. Filley, A. C. Ho, A. Santos, A. B. Safran, A. Arditi, L. V. D. Priore, and R. J. Greenberg: Ophthalmology **119** (2012) 779.
6) S. Klauke, M. Goertz, S. Rein, D. Hoehl, U. Thomas, R. Eckhorn, F. Bremmer, and T. Wachtler: Invest. Ophthalmol. Visual Sci. **52** (2011) 449.
7) A. Y. Chow, V. Y. Chow, K. H. Packo, J. S. Pollack, G. A. Peyman, and R. Schuchard: Arch. Ophthalmol. **122** (2004) 460.
8) T. Tanaka, K. Sato, K. Komiya, T. Kobayashi, T. Watanabe, T. Fukushima, H. Tomita, H. Kurino, M. Tamai, and M. Koyanagi: IEDM Tech. Dig., 2007, p. 1015.
9) S. K. Kelly, D. B. Shire, P. Doyle, M. D. Gingerich, W. A. Drohan, J. F. Rizzo, J. Chen, L. S. Theogarajan, S. F. Cogan, and J. L. Wyatt: Proc. 2nd Int. Symp. Applied Sciences in Biomedical and Communication Technologies, 2009, p. 1.
10) T. Tokuda, Y. Takeuchi, Y. Sagawa, T. Noda, K. Sasagawa, K. Nishida, T. Fujikado, and J. Ohta: IEEE Trans. Biomed. Circuits Syst. **4** (2010) 445.
11) M. N. Shivdasani, C. D. Luu, R. Cicione, J. B. Fallon, P. J. Allen, J. Leuenberger, G. J. Suaning, N. H. Lovell, R. K. Shepherd, and C. E. Williams: J. Neural Eng. **7** (2010) 036008.
12) M. R. Behrend, A. K. Ahuja, M. S. Humayun, R. H. Chow, and J. D. Weiland: IEEE Trans. Neural Syst. Rehabil. Eng. **19** (2011) 436.
13) W. Poppendieck, K. P. Koch, S. Steltenkamp, and K. P. Hoffmann: Int. Federation for Medical and Biological Engineering, 2009, p. 162.
14) M. S. Humayun, E. D. Juan, Jr., J. D. Weiland, G. Dagnelie, S. Katona, R. Greenberg, and S. Suzuki: Vision Res. **39** (1999) 2569.
15) A. Rothermel, L. Liu, N. P. Aryan, M. Fischer, J. Wuenschmann, S. Kibbel, and A. Harscher: IEEE J. Solid-State Circuits **44** (2009) 290.
16) S. F. Cogan: Annu. Rev. Biomed. Eng. **10** (2008) 275.
17) J. D. Weiland, D. J. Anderson, and M. S. Humayun: IEEE Trans. Biomed. Eng. **49** (2002) 1574.
18) F. Gekeler, K. Kobuch, H. N. Schwahn, A. Stett, K. Shinoda, and E. Zrenner: Graefe's Arch. Clin. Exp. Ophthalmol. **242** (2004) 587.
19) A. Y. Chow and V. Y. Chow: Neurosci. Lett. **225** (1997) 13.
20) S. Ghosh and O. Inganäsz: J. Electrochem. Soc. **147** (2000) 1872.

 © 2013 The Japan Society of Applied Physics

Contents lists available at SciVerse ScienceDirect

Sensors and Actuators B: Chemical

journal homepage: www.elsevier.com/locate/snb

High-speed chemical imaging system based on front-side-illuminated LAPS

Akinori Itabashi[a], Naoki Kosaka[b], Ko-ichiro Miyamoto[a,*], Torsten Wagner[a], Michael J. Schöning[c,d], Tatsuo Yoshinobu[a,b]

[a] Department of Electronic Engineering, Tohoku University, 6-6-05 Aza-Aoba, Aramaki, Aoba-ku, Sendai 980-8579, Japan
[b] Department of Biomedical Engineering, Tohoku University, 6-6-05 Aza-Aoba, Aramaki, Aoba-ku, Sendai 980-8579, Japan
[c] Institute of Nano- and Biotechnologies, Aachen University of Applied Sciences, Heinrich-Mußmann Straße 1, 52428 Jülich, Germany
[d] Peter Grünberg Institute (PGI-8), Research Centre Jülich, 52425 Jülich, Germany

ARTICLE INFO

Article history:
Received 15 July 2012
Received in revised form 1 March 2013
Accepted 7 March 2013
Available online 16 March 2013

Keywords:
Chemical imaging sensor
Light-addressable potentiometric sensor
LAPS
pH distribution
Front-side illumination

ABSTRACT

The chemical imaging sensor is a semiconductor-based chemical sensor that can visualize the spatial distribution of specific ions on the sensing surface. The conventional chemical imaging system based on the light-addressable potentiometric sensor (LAPS), however, required a long time to obtain a chemical image, due to the slow mechanical scan of a single light beam. For high-speed imaging, a plurality of light beams modulated at different frequencies can be employed to measure the ion concentrations simultaneously at different locations on the sensor plate by frequency division multiplex (FDM). However, the conventional measurement geometry of back-side illumination limited the bandwidth of the modulation frequency required for FDM measurement, because of the low-pass filtering characteristics of carrier diffusion in the Si substrate. In this study, a high-speed chemical imaging system based on front-side-illuminated LAPS was developed, which achieved high-speed spatiotemporal recording of pH change at a rate of 70 frames per second.

© 2013 Elsevier B.V. All rights reserved.

1. Introduction

The light-addressable potentiometric sensor (LAPS) [1] belongs to the family of semiconductor-based chemical sensors with an electrolyte–insulator–semiconductor (EIS) structure. The width of the depletion layer in the Si substrate responds to the ion concentration on the sensing surface, and the variation of its capacitance is read out in the form of AC photocurrent induced by illumination of the sensor plate with a modulated light. The most advantageous point of the LAPS measurement is that the measurement area can be defined by illumination. Based on this addressability of LAPS, we developed the chemical imaging sensor [2], which could visualize the two-dimensional distribution of specific ions in the solution on the sensing surface.

In a conventional chemical imaging system based on LAPS, a scanning light beam was used to obtain a two-dimensional map of the ion concentration. Due to the mechanical scan, however, a typical scan time to acquire a chemical image at a resolution of 128 × 128 pixels was about 3 min, which was too long to analyze the dynamics of chemical reactions.

Frequency division muliplex (FDM) [3] is one of the methods for high-speed chemical imaging, in which a plurality of light beams modulated at different frequencies are employed to read out the ion concentrations at different locations in parallel as shown in Fig. 1. In this case, the photocurrent signal is a superposition of all frequency components and each component can be individually extracted by Fourier analysis. Based on FDM-LAPS, we developed a chemical image scanner system [4], which employed a linear array of 16 LEDs to scan a chemical image at a resolution of 16 × 128 pixels. The scan time was reduced to 6.4 s, which, however, was still slow in comparison, for example, to the pH imaging sensor based on the charge coupled device (CCD) technology [5,6]. In our previous study, we developed a chemical movie recording system based on FDM and a two-dimensional array of LEDs. Using a two-dimensional array of LEDs as a light source, the slow mechanical scan of the conventional system was replaced by much faster electrical switching and a high-speed imaging at a frame rate of 10 fps (frames per second) was achieved [7].

In FDM, the required bandwidth of the modulation frequency is given by (number of light beams) × (frequency spacing) and the time window of Fourier analysis or the sampling time must be at least as long as 1/(frequency spacing). For high-speed chemical imaging, therefore, a wide bandwidth of frequency is required to increase the multiplicity and to reduce the time window. Here, two different geometries are possible in LAPS measurement [8] as shown in Fig. 2. Those are front-side and back-side illuminations,

* Corresponding author.
E-mail addresses: k-miya@ecei.tohoku.ac.jp, k.miyamoto.1979@gmail.com (K.-i. Miyamoto).

0925-4005/$ – see front matter © 2013 Elsevier B.V. All rights reserved.
http://dx.doi.org/10.1016/j.snb.2013.03.016

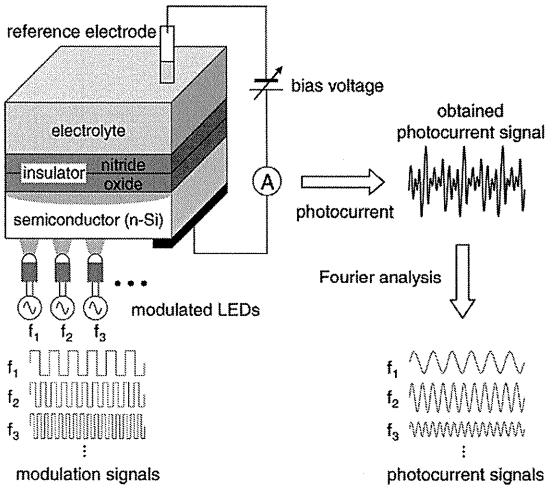

Fig. 1. Diagram of simultaneous measurement at multiple points on the sensing surface by frequency division multiplex.

in which the front-side or the back-side surface of the sensor plate is illuminated, respectively, by the modulated light. In the case of back-side illumination, which is the geometry of conventional LAPS measurement, the modulation frequency is limited by the low-pass filtering characteristics of carrier diffusion across the sensor plate. In front-side illumination, on the other hand, higher frequencies can be used, because photocarriers are directly generated and separated inside the depletion layer and no diffusion process is involved [8]. Front-side illumination, however, has some restrictions. For front-side illumination, the modulated light beam has to transit through the object to be measured. The object, therefore, must be light-transmissive and the distribution of the light transmittance of the object must be invariant while the pH distribution changes.

In this study, we developed a high-speed chemical imaging system based on the combination of FDM, a two-dimensional array of LEDs and front-side illumination. Front-side illumination allowed a wide bandwidth of the modulation frequency required for high-speed measurement by FDM. The developed system achieved high-speed chemical imaging at about 70 fps and provided real-time observation of a spatiotemporal change of pH distribution in a solution.

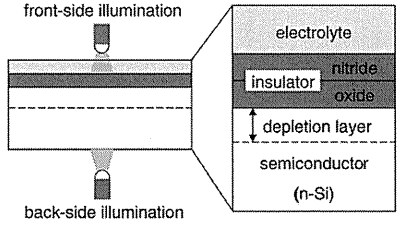

Fig. 2. Two different geometries of the LAPS measurement: front-side and back-side illuminations.

2. Experimental

Fig. 3(a) shows a schematic view of the high-speed chemical imaging system developed in this study. This system consists of a sensor plate, a two-dimensional array of LEDs (LED matrix), an oscillator array and a control PC with measurement software.

2.1. Sensor plate

The sensor plate (36 mm × 36 mm) used in this study was made of n-type Si wafer with a thickness of 200 μm and a resistivity of 10–20 Ω cm. The top surface of the sensor plate was covered with a 50 nm-thick thermal SiO_2 layer to obtain a semiconductor–insulator interface with low trap density and subsequently a 100 nm-thick Si_3N_4 layer deposited by low-pressure chemical vapor deposition (LP-CVD). The surface of the Si_3N_4 layer functions as a pH-sensitive surface when brought into contact with the sample solution. A thin ohmic electrode was deposited on the back-side of the sensor plate.

2.2. LED matrix

Fig. 3(b) shows the top view of the LED matrix with 7 × 5 LEDs (TA07-11SRWA, Kingbright Elec. Co., Ltd.) installed above the sensor plate as a light source. The peak wavelength and the intensity of illumination are 660 nm and 24 mcd, respectively. The light-emitting face of the LED matrix is immersed directly into the sample solution. The distance between the LED matrix and the sensor surface, or the thickness of the solution layer, through which the light has to pass, is about 0.6 mm. Five different frequencies are input to each column of the LED matrix and five points on the sensor surface corresponding to the five LEDs on one line are measured in parallel. By electrically switching the illuminating lines from the first to the seventh row in sequence, ion concentration values at all 35 points are obtained without mechanical scan.

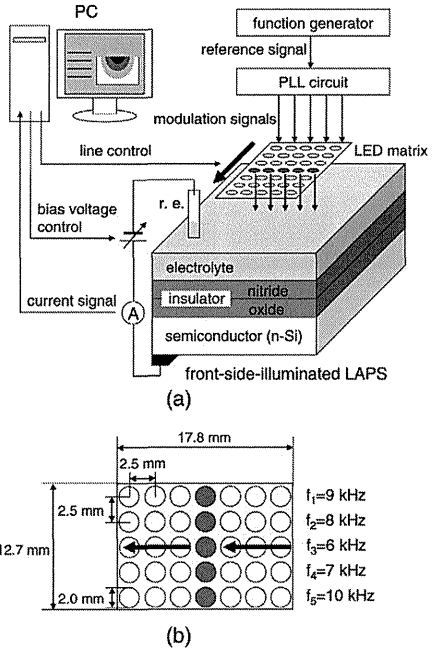

Fig. 3. (a) Schematic view of the high-speed chemical imaging system based on front-side-illuminated LAPS, and (b) top view of the LED matrix used in this system.

2.3. Oscillator array

Five modulation frequency signals of 6, 7, 8, 9 and 10 kHz are generated as integer multiples of the reference frequency of 100 Hz by a 5-channel phase-locked loop (PLL) synthesizer.

2.4. PC and software

A software developed with LabVIEW (National Instruments Corp.) is used to control the bias voltage between the reference electrode and the sensor plate, to switch a line of the LED matrix in sequence, to measure the photocurrent, to calculate each frequency component by the method described in our previous paper [4] and to display the obtained chemical image.

3. Results and discussion

3.1. Front-side vs. back-side illumination

To compare the performance of front-side and back-side illuminations, I–V curves were measured in both geometries at various frequencies in the range of 5–110 kHz. The test solution was a pH 7 buffer solution, and the sampling frequency and the sampling time were 500 kHz and 20 msec, respectively. The bias voltage was swept from −2.0 to 0.0 V at a step of 10 mV.

Fig. 4(a) compares the I–V curves obtained with front-side and back-side illuminations, respectively, at a modulation frequency of 10 kHz. In the case of back-side illumination, electron–hole pairs are generated near the back-side surface of the Si substrate and the photocarriers reach the depletion layer by diffusion. While only those photocarriers separated in the depletion layer contribute to the external photocurrent, a large part of generated photocarriers are lost by recombination during the diffusion process, and the obtained photocurrent becomes small. In the case of front-side illumination, on the other hand, the electron–hole pairs are generated and separated directly in the depletion layer, and therefore, a larger photocurrent is obtained [8].

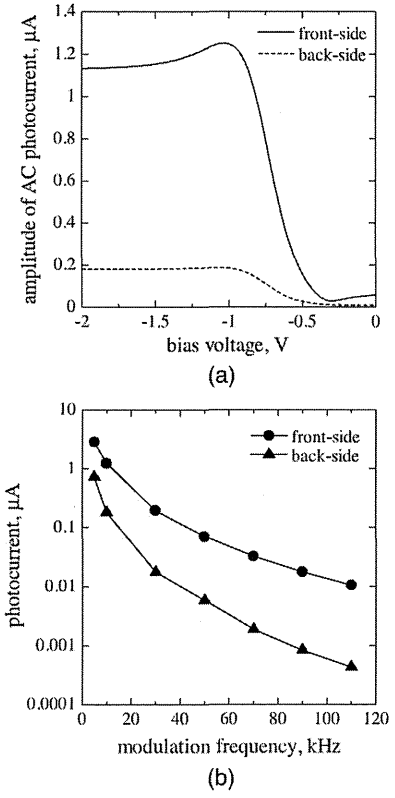

Fig. 4. (a) I–V curves for front-side or back-side illumination in the case of LED light modulated at 10 kHz, and (b) magnitudes of photocurrent as a function of the modulation frequency for front-side and back-side illuminations.

Fig. 4(b) shows the magnitude of photocurrent as a function of the modulation frequency for front-side and back-side illuminations, where the magnitude was defined as the difference of the maximum and minimum values of photocurrent in the I–V curve. Although the photocurrent decreases with the modulation frequency in both geometries, the decrease in back-side illumination is steeper than that in front-side illumination, which can be explained in terms of the low-pass filtering effect of carrier diffusion in the semiconductor layer.

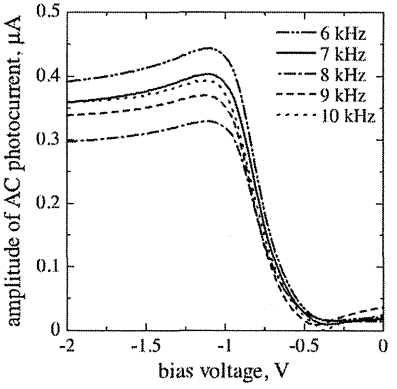

Fig. 5. I–V curves for simultaneous measurement by frequency division multiplex on one line of the LED matrix with 5 LEDs modulated at 6, 7, 8, 9 and 10 kHz.

These results demonstrate that front-side illumination, which offers a wider bandwidth of the modulation frequency, is more suitable for high-speed chemical imaging.

3.2. Parallel measurement

As a test of parallel measurement with FDM, five I–V curves were simultaneously obtained with five LEDs on the fourth row of the LED matrix modulated at different frequencies of 6, 7, 8, 9 and 10 kHz. The test solution was again a pH 7 buffer solution, the sampling frequency and sampling time were 200 kHz and 50 ms, and the bias voltage was swept from −2.0 to 0.0 V with a step of 10 mV.

Fig. 5 shows the amplitudes of the photocurrent of each frequency component as functions of the bias voltage. It was demonstrated that five I–V curves at different positions on the sensing surface could be simultaneously obtained. As observed in Fig. 5, however, the heights of I–V curves may differ due to the frequency-dependence of the photocurrent, variation of light intensities among LEDs and non-uniformity of the sensor plate. Therefore, it is necessary to normalize the measured photocurrent at each pixel to compensate for such artifacts.

3.3. Chemical imaging

In a LAPS measurement, the ion concentration in the sample solution is calculated from the shift of the I–V curve along the voltage axis. In chemical imaging, however, measurement of I–V curves at all pixels would be too time-consuming, and therefore, the photocurrent under a constant bias voltage is recoded at each pixel and converted into the ion concentration values. In the case of a sensor plate with n-type semiconductor, the photocurrent decreases for lower pH values and increases for higher pH values under a fixed bias voltage. To compensate for the variation of photocurrent as was seen in Fig. 5, the photocurrent value measured at each pixel was normalized to the photocurrent value measured in advance for a uniform solution.

3.3.1. Chemical imaging of pH buffer solutions

As a test of pH imaging, chemical images of a series of buffer solutions of pH 4–10 (Titrisol®, Merck KGaA, Germany) were acquired. The photocurrent value at each pixel was normalized to the photocurrent values of uniform pH 7 buffer solution. Fig. 6 shows a series of chemical images for pH 4–10 buffer solutions. As shown in Fig. 6, these chemical images are almost uniform in color representations corresponding to the uniformity of buffer solutions. Fig. 7 shows the average of the normalized photocurrent over all 35 pixels as a function of the pH value. A linear dependence of the normalized photocurrent on the pH value was observed with a slope of about 0.26/pH. This experimental result indicates that the developed system is capable of imaging pH values in the range of pH 4–10.

3.3.2. High-speed chemical imaging of pH change

Using the developed chemical imaging system based on front-side-illuminated LAPS, a high-speed chemical imaging experiment was performed to observe the spatiotemporal changes of pH values caused by injection of acid into a solution. The sampling frequency and the sampling time per line were 400 kHz and 10 ms. It takes, therefore, 70 ms to scan a frame of 7 lines, which corresponds to a frame rate of about 14 fps.

Fig. 8(a) shows the snapshots of 14 fps chemical imaging experiment, in which 0.2 ml of 0.1 M HCl solution was injected into 2.0 ml of 0.1 M NaCl solution at a constant rate of 0.13 ml/s. Spreading of acidic area by injection of HCl was observed in real time. Fig. 8(b) shows an experiment, in which 0.2 ml of 0.1 M HCl was injected into 2.0 ml of neutral phosphate buffer solution (pH 6.86) at a constant

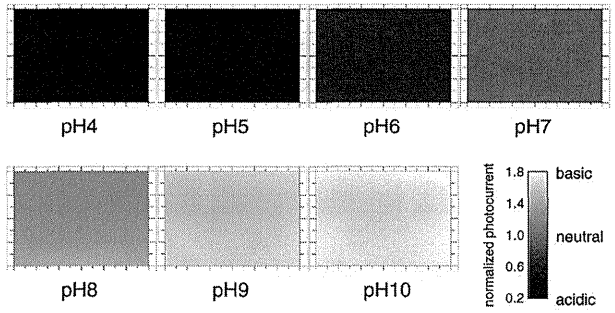

Fig. 6. Chemical images corresponding to different pH values (pH 4–10). These images were generated by interpolating 35 measurement values.

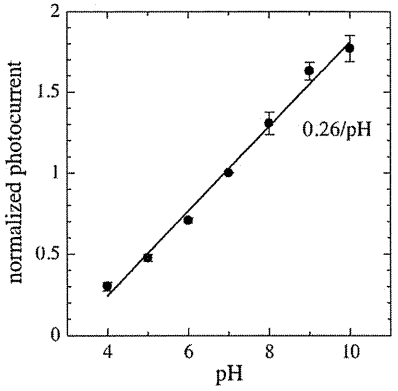

Fig. 7. The normalized photocurrent as a function of the pH value. The black circle is the average of the normalized photocurrent over all 35 pixels and the error bar shows the standard deviation.

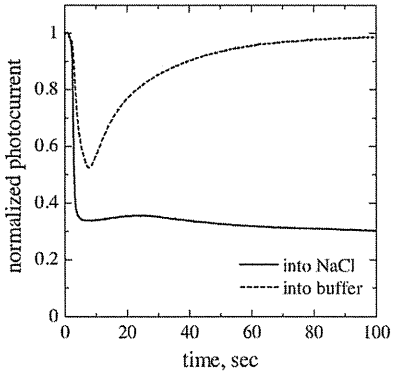

Fig. 9. Time responses of the normalized photocurrent corresponding to the pH value at the center of the LED matrix after injecting HCl solution into NaCl solution or neutral phosphate buffer solution.

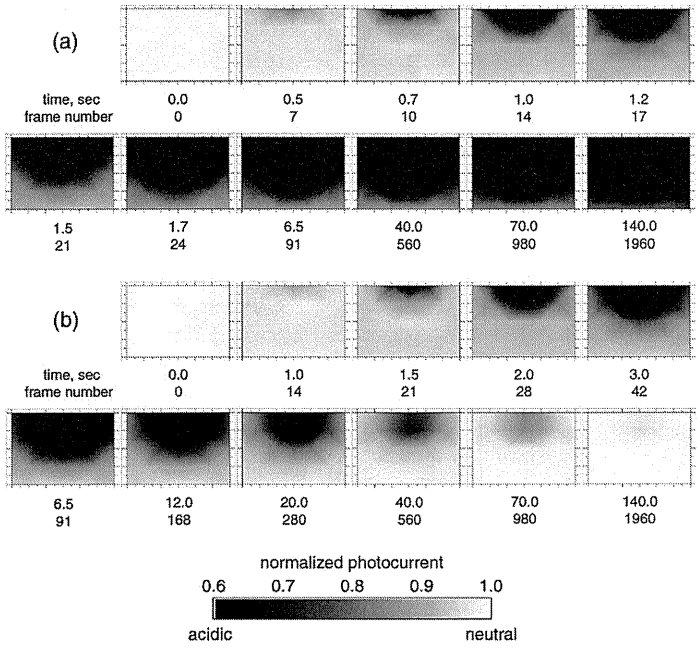

Fig. 8. Snapshots of 14 fps chemical imaging experiment. Spatiotemporal change of pH distribution was recorded after injecting HCl solution into (a) NaCl solution or (b) neutral phosphate buffer solution. These images were generated by interpolating 35 measurement values.

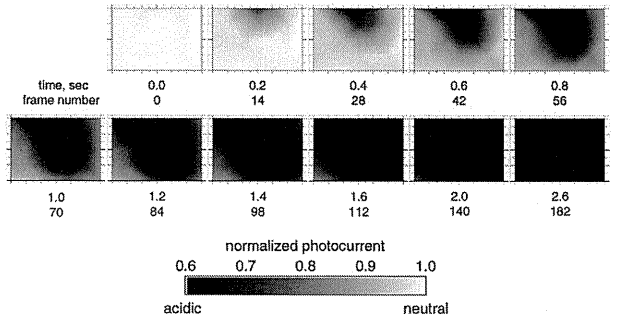

Fig. 10. Snapshots of 70 fps chemical imaging experiment. Spatiotemporal change of pH distribution was recorded after injecting HCl solution into NaCl solution. These images were generated by interpolating 35 measurement values.

rate of 0.13 ml/s. After spreading of acidic area, shrinking of acidic area due to the buffering action,

$$H^+ + HPO_4^{2-} \rightarrow H_2PO_4^-$$

was observed. These experimental results demonstrate the possibility of spatiotemporal recording of chemical reactions by the developed system.

Fig. 9 shows the temporal changes of the normalized photocurrent recorded at the center of the LED matrix. In the case of NaCl solution, the normalized photocurrent decreased rapidly during injection of HCl solution and then decreased slowly by diffusion of hydrogen ions toward the center. In the case of phosphate buffer solution, on the other hand, the normalized photocurrent returned to the initial state due to the buffering action after the decrease by injection of HCl solution.

Chemical imaging at even higher speed is possible by reducing the sampling time per line from 10 ms to 2 ms. In this case it takes 14 ms to scan a frame of 7 lines, which corresponds to a frame rate of about 70 fps. Fig. 10 shows the snapshots of 70 fps chemical imaging experiment with a sampling frequency of 400 kHz. In this experiment, 0.3 ml of 0.1 M HCl solution was injected into 2.0 ml of 0.1 M NaCl solution at a constant rate of 0.13 ml/s. Rapid change of pH distribution was recorded as a smooth movie.

Due to reduction of the measurement time, the measurement error in the 70 fps experiment is larger than that in the 14 fps experiment. The standard deviation (averaged over all 35 pixels) of the normalized photocurrent measured for a solution of constant pH was 0.00182 and 0.00503 in the 14 fps and 70 fps experiments, respectively. Converting these values into pH deviation, the measurement accuracy at 14 fps was about ±0.007 pH and that at 70 fps was about ±0.02 pH. The measurement error in the 70 fps experiment, therefore, was about three times larger than that in 14 fps. Thus, the measurement condition has to be selected depending on the purpose of the measurement.

4. Conclusion

In this study, a high-speed chemical imaging system based on front-side-illuminated LAPS was developed using a two-dimensional array of LEDs. It was demonstrated that front-side illumination was more suitable for high-speed chemical imaging, which would require a wide bandwidth of the modulation frequency. Using the developed system, a rapid change of pH distribution could be visualized by acquiring chemical images at 70 fps.

A chemical imaging system with an even higher temporal resolution is under development, which allows parallel access to all pixels using a two-dimensional array of LEDs modulated independently at different frequencies. Such a high-speed system combined with an optical fiber bundle for arranging measurement pixels at higher density would be useful for analysis of chemical reactions in more detail and applications in the field of biology.

Acknowledgments

This work was supported by JSPS Grant-in-Aid for Scientific Research (B) (contract no. 24310098). A part of this research was carried out at the Machine Shop Division of Fundamental Technology Center, Research Institute of Electrical Communication, Tohoku University.

References

[1] D.G. Hafeman, J.W. Parce, H.M. McConnell, Light-addressable potentiometric sensor for biochemical systems, Science 240 (1988) 1182–1185.
[2] M. Nakao, T. Yoshinobu, H. Iwasaki, Scanning-laser-beam semiconductor pH-imaging sensor, Sensors and Actuators B 20 (1994) 119–123.
[3] Q. Zhang, P. Wang, W.J. Parak, M. George, G. Zhang, A novel design of multi-light LAPS based on digital compensation of frequency domain, Sensors and Actuators B 73 (2001) 152–156.
[4] K. Miyamoto, Y. Kuwabara, S. Kanoh, T. Yoshinobu, T. Wagner, M.J. Schöning, Chemical image scanner based on FDM-LAPS, Sensors and Actuators B 137 (2009) 533–538.
[5] K. Sawada, S. Miura, K. Tomita, T. Nakanishi, H. Tanabe, M. Ishida, T. Ando, Novel CCD-based pH imaging sensor, IEEE Transactions on Electronic Devices 46 (1999) 1846–1849.
[6] T. Hizawa, K. Sawada, H. Takao, M. Ishida, Fabrication of a two-dimensional pH image sensor using a charge transfer technique, Sensors and Actuators B 117 (2006) 509–515.
[7] K. Miyamoto, N. Kosaka, T. Wagner, T. Yoshinobu, High-resolution and high-speed chemical imaging sensor based on optical fiber array, Extended Abstracts of 2012 International Conference on Solid State Devices and Materials (SSDM2012), pp. 368–369.
[8] M. Sartore, M. Adami, C. Nicolini, L. Bousse, S. Mostarshed, D. Hafeman, Minority carrier diffusion length effects on light-addressable potentiometric sensor (LAPS) devices, Sensors and Actuators A 32 (1992) 431–436.

Biographies

Akinori Itabashi was born in Miyagi, Japan, in 1989. He received BE and ME from Department of Electronic Engineering of Tohoku University in 2011 and 2013, respectively. His research subject is on the development of chemical imaging sensor based on the light-addressable potentiometric sensor.

Naoki Kosaka was born in Aomori, Japan, in 1987. He received BE from Department of Electronic Engineering of Tohoku University in 2010, and received ME from

the Graduate School of Biomedical Engineering, Tohoku University in 2012. His research subject is on the development of chemical imaging sensor based on the light-addressable potentiometric sensor.

Ko-ichiro Miyamoto was born in Yamaguchi, Japan, in 1979. He received BE, ME and PhD degrees from Tohoku University in 2002, 2004 and 2006, respectively. His PhD degree is for his study on the bio-molecular sensing using infrared absorption spectroscopy. Since 2006, he is an assistant professor in the Department of Electronic Engineering, Tohoku University. His research subject is on the application of silicon-based chemical sensors for bio-molecular sensing.

Torsten Wagner was born in Mönchengladbach, Germany, in 1978. He received his diploma in 2003 in Electrical Engineering from the University of Applied Sciences Aachen, his master of science in 2003 in model simulation and control from the Coventry University in UK, and his doctoral degree (PhD) in 2008 from the Philips University Marburg in cooperation with the University of Applied Sciences Aachen. His research subjects concern chemical sensors, especially the light-addressable potentiometric sensor and sensor-signal processing. He received a scholarship (2008–2010) from the Japanese Society for the Promotion of Sciences (JSPS) to work at the Tohoku University in Japan, at which he became 2010 an assistant professor.

Michael J. Schöning received his diploma degree in Electrical Engineering (1989) and his PhD in the field of semiconductor-based microsensors for the detection of ions in liquids (1993), both from the Karlsruhe University of Technology. In 1989, he jointed the Institute of Radiochemistry at the Research Centre Karlsruhe. Since 1993, he has been with the Institute of Thin Films and Interfaces (now, Institute of Bio and Nanosystems) at the Research Centre Jülich, and since 1999 he was appointed as full Professor at Aachen University of Applied Sciences, Campus Jülich. Since 2006, he serves as a director of the Peter-Grünberg Institute (PGI-8) at the Aachen University of Applied Sciences. His main research subjects concern silicon-based chemical and biological sensors, thin-film technologies, solid-state physics, microsystem and nano(bio-)technology.

Tatsuo Yoshinobu was born in Kyoto, Japan, in 1964. He received BE, ME, and PhD degrees in electrical engineering from Kyoto University in 1987, 1989, and 1992, respectively, for his study on gas source molecular beam epitaxy of silicon carbide. In 1992, he joined the Institute of Scientific and Industrial Research, Osaka University, where he started the development of silicon-based chemical sensors. From 1999 to 2000, he was a guest scientist at the Research Centre Jülich, Germany. Since 2005, he is a professor for Electronic Engineering at Tohoku University, Sendai, Japan. Since 2008, he is also a professor at the Graduate School of Biomedical Engineering, Tohoku University.

THE JOURNAL OF ALTERNATIVE AND COMPLEMENTARY MEDICINE
Volume 19, Number 5, 2013, pp. 416–419
© Mary Ann Liebert, Inc.
DOI: 10.1089/acm.2012.0217

Brief Effect of Acupoint Stimulation Using Focused Ultrasound

Noriko Tsuruoka, MS,[1] Masashi Watanabe, MA,[2] Shin Takayama, MD, PhD,[2] Takashi Seki, MD, PhD,[2] Tadao Matsunaga, PhD,[3] and Yoichi Haga, MD, PhD[1]

Abstract

Background: Acupuncture is used worldwide in medical treatment. However, needle insertion damages the skin and patients sometimes feel pain. To avoid such drawbacks, an acupoint stimulation device using focused ultrasound has been developed. Ultrasound stimulation does not damage the skin like acupuncture does because ultrasound can deliver vibration energy to soft tissues noninvasively.
Objectives: The aim of this study was to clarify the effect of acupoint stimulation using focused ultrasound.
Subjects: Fifty (50) healthy volunteers (40 males and 10 females) were included in this experiment.
Design: Subjects were randomly assigned to two groups. LR-3 was stimulated bilaterally for 36 seconds by focused ultrasound and conventional acupuncture. Brachial artery blood flow volume was monitored by an ultrasound with an echo-tracking system. The hemodynamic parameters were measured before, during, and 30, 60, 180 seconds after stimulation.
Results: During stimulation, the blood flow volume of the acupuncture stimulation group decreased significantly ($p<0.05$) compared with resting value, but that of the focused ultrasound stimulation group did not decrease. Blood flow volume of both groups increased gradually and showed significant increase at 180 seconds after stimulation ($p<0.05$).
Conclusions: Blood flow volume was increased significantly by both focused ultrasound stimulation and conventional acupuncture. Although a significant decrease of blood flow volume during acupuncture stimulation was observed, no such decrease was observed during ultrasound stimulation. Findings of the present study show that noninvasive stimulation of acupoints by focused ultrasound is as effective as conventional acupuncture in blood flow volume of the brachial artery.

Introduction

Because ultrasound can deliver vibration energy to soft tissues noninvasively, ultrasound has been applied to diagnostic imaging[1,2] and therapeutic applications.[3–5] To use ultrasound for acupoint stimulation, a stimulation device was developed using focused ultrasound.[8] This device stimulates only one point (about 1 mm^3) of tissue. Appropriate stimulation intensity and pattern can be obtained by changing the driving voltage and its pattern.

Insertion of needles in acupuncture damages the skin,[9,10] but ultrasound stimulation does not. Thus, ultrasound stimulation has a smaller risk of infection and users do not feel any pain during stimulation. Focused ultrasound stimulation uses almost the same intensity as ultrasound physical therapy (1–3 W/cm^2).[7] Temperature increase at the focal point can be suppressed by changing the supply voltage and waveform. For this reason, ultrasound stimulation can be considered safer than acupuncture.

The size of the ultrasound transducer is about 6 mm in diameter, small enough to be easily placed the skin during daily life. Users can switch the device on whenever they want to stimulate acupoints.

The aim of this study was to clarify the effect of acupoint stimulation using focused ultrasound.

Materials and Methods

Methods

Fifty (50) healthy volunteers (40 males and 10 females) were included in this experiment. The study protocol was approved by the Ethics Committee of Tohoku University Graduate School of Medicine, and written informed consent for participation was given by all of the subjects. Subjects

[1]Graduate School of Biomedical Engineering, Tohoku University, Sendai, Japan.
[2]Graduate School of Medicine, Tohoku University, Sendai, Japan.
[3]Micro System Integration Center (μSIC), Tohoku University, Sendai, Japan.

Table 1. Characteristics of the Subjects in Groups A and B

	Group A	*Group B*	p-*Value*
Age (years)	29.12±10.10	31.84±5.94	0.13
Sex (male:female)	20:5	20:5	—
Weight (kg)	63.61±8.23	66.76±10.62	0.12
Height (cm)	170.72±7.41	170.38±8.49	0.44
Body surface area (m^2)	1.74±0.14	1.77±0.17	0.23
Blood flow volume of brachial artery at rest (mL/s/m^2)	0.68±0.35	0.71±0.45	0.41

Values are presented as the mean±standard deviation.

were randomly assigned to group A (focused ultrasound stimulation) or group B (conventional acupuncture). The clinical profile of each group is shown in Table 1, and the protocol of this study is shown in Figure 1. The protocol was made referring to reports by Takayama et al.[11,12]

Each subject rested for 10 minutes in a supine position. At the end of the 10-minute rest period, measurement of brachial blood flow volume was started. LR-3 was stimulated bilaterally for 36 seconds. Group A subjects were stimulated by focused ultrasound using the focused ultrasound device that was fabricated, and group B subjects were stimulated by conventional acupuncture.

In order to compare the effect of focused ultrasound stimulation with that of acupuncture as shown by numerical value, blood flow volume of the brachial artery was measured. The LR-3 acupoint is the primary acupoint on the Liver meridian and has the functions of "smoothing the Liver" and "regulating the Blood" in Traditional Chinese Medicine. The effect on the radial artery by stimulation of LR-3 with acupuncture has been reported.[11,12] Thus, LR-3 was stimulated to confirm the effect of focused ultrasound stimulation on blood flow volume of the brachial artery.

Blood flow volume was measured by an ultrasound system (Prosound α10®, Aloka Co., Ltd., Japan) at 30, 60, and 180 seconds after the stimulation. In order to reduce the influence of respiration on blood flow volume, the subjects were asked to breathe every 6 seconds during the experiment, and blood flow volume was averaged for 6 seconds at the measuring point.

Focused ultrasound stimulation

To produce focused ultrasound, the device shown in Figure 2 was fabricated. Focused ultrasound was produced by a concave-shaped PZT (lead zirconate titanate, $Pb(Zr_x,Ti_{1-x})O_3$) transducer.[8] The diameter of the device is 5.5 mm and its focal point is 9 mm from the device. In this method, the focal point is set at a depth of 5 mm from the skin surface. This is almost the same depth as insertion of an acupuncture needle. The ultrasound intensity at the focal point was set at about 2.38 W/cm^2 by applying a 20 V_{p-p} sine wave of resonance frequency (1.83 MHz) to the device. Before the experiment, the temperature increase at the focal point was measured in an agar phantom by a thermocouple. The rise of temperature under the condition of this experiment (2.38 W/cm^2, 36 seconds) was less than 1°C.

Acupuncture stimulation

Acupuncture was performed by a licensed acupuncturist. A disposable fine stainless steel needle (diameter: 0.16 mm; length: 40 mm; Seirin Co., Ltd., Japan) was inserted at LR-3 bilaterally and maintained at a depth of 5–10 mm during the experiment. After the needle was inserted, stimulation (rotating the needles manually within an angle of 90°) was performed for 18 seconds.

Statistics

Statistical analysis was performed with SPSS software. Repeated-measures ANOVA, followed by Dunnett's *post hoc* test were used for statistical comparison between the measurement points. Two-way ANOVA was used for statistical comparison between groups A and B. Results are presented as the mean±standard deviation and $p<0.05$ was used to indicate significance for all statistical analysis.

Results

Table 1 shows the characteristics of the subjects in groups A and B. There were no significant differences in age, sex, weight, height, body surface, or blood flow volume of the brachial artery before stimulation.

The blood flow volume was determined as milliliters per second per square meter and calculated in relation to resting value as percent change. The change of blood flow volume is shown in Figure 3. The blood flow volume of group B decreased significantly during acupuncture ($p<0.05$) compared with resting value, but that of group A did not decrease, during ultrasound stimulation. After stimulation, blood flow volume of groups A and B changed similarly. They increased gradually and showed a significant increase at 180 seconds after stimulation ($p<0.05$). There was a significant difference in the change of blood flow volume between groups A and B ($p=0.012$).

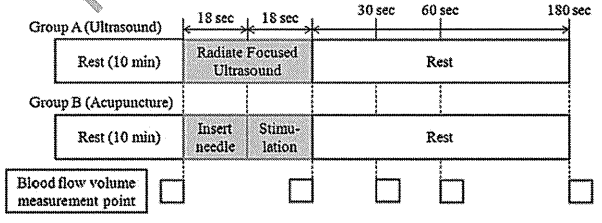

FIG. 1. Protocol of the experiment. Measurement of blood flow volume was performed before, during, and 30, 60, and 180 seconds after acupoint stimulation. Group A subjects were stimulated by focused ultrasound, and Group B subjects were stimulated by acupuncture.

For Review Only
Not Intended for Distribution
Reproduction

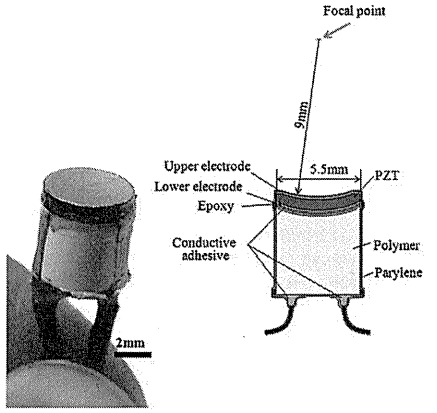

FIG. 2. Photograph and cross-sectional view of focused ultrasound device. PZT, lead zirconate titanate.

Burn injury, bleeding, skin denaturation, and infection by ultrasound stimulation did not occur in group A subjects. Similarly, neither infection nor bleeding by acupuncture stimulation was a problem in group B subjects.

Discussion

During stimulation, the blood flow volume of every group B subject temporarily decreased. Although almost none of the subjects felt pain, nociceptive stimulation by needle insertion might cause transient contraction of the peripheral artery. There was no significant decrease of blood flow volume with focused ultrasound stimulation (group A) during stimulation. This might suggest that focused ultrasound stimulation did not result in nociceptive stimulation. Several stimulations are used to generate a signal input from the skin, and the information is transmitted to the spinal area and the central nervous system. The mechanisms of acupuncture reaction have explained by spinal level and supraspinal mechanisms. The physiological mechanisms of decreased and increased blood flow volume in the upper limb by the stimulations applied from the skin are related to a peripheral vascular resistance due to an instantaneous increase and decrease in sympathetic tone. Generally, needle acupuncture is interpreted as nociceptive stimulation. On the other hand, ultrasound stimulation might be interpreted as thermal and vibratory stimulation. Because captured peripheral nerves by the stimulations are different between acupuncture and ultrasound stimulation, the physiological reaction might be different.

At 180 seconds after stimulation, a significant increase of blood flow volume occurred in group B. This change of blood flow volume suggests that stimulation by acupuncture caused peripheral artery vasodilation. Takayama et al. have reported the effect of acupuncture on blood flow volume of the brachial artery.[12] They suggested that acupuncture at LR-3 can affect the sympathetic tone of the upper limbs. In group A, a significant increase of blood flow volume was also shown at 180 seconds after stimulation. This proves that like conventional acupuncture, stimulation by focused ultrasound at an acupoint is effective. Two factors are thought to be involved in the stimulation of an acupoint using focused ultrasound. One is a physical factor and the other is a thermal factor.[7,13] Body tissue at the focal point might be vibrated by acoustic pressure of focused ultrasound. This causes physical stimulation like that caused by acupuncture. If the ultrasound energy is changed to thermal energy in body tissue at the focal point, the temperature of the focal point rises, which causes thermal stimulation like moxibustion. The temperature rise of our device was measured in an agar phantom before the experiment. Under the present experimental conditions (supply voltages, waveform, stimulation time), there was no temperature rise at the focal point. Thus, it is suggested that focused ultrasound caused only physical stimulation at the acupoints in this experiment.

When inserting an acupuncture needle, the needle damages the skin and patients sometimes feel pain.[9,10] During acupoint stimulation with ultrasound, however, patients do not feel pain, including nociceptive pain. Ultrasound stimulation does not damage the skin, and entails no risk of bleeding.

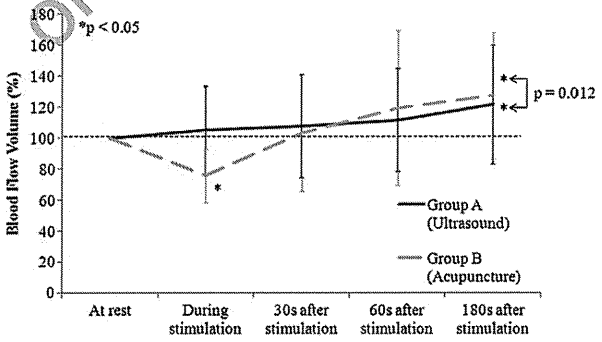

FIG. 3. Percent change of blood flow volume of brachial artery. Values are presented as the mean ± standard deviation, and $^*p < 0.05$ versus before stimulation.

In a healthy person, the effect of focused ultrasound stimulation on blood flow is similar to acupuncture. Focused ultrasound stimulation has potential for use as noninvasive acupoint stimulation in clinical application. Further study will be needed to investigate the effects in clinical conditions.

Limitations

The results should be treated with caution, given that this is a pilot study with no placebo control intervention and a short examination time. There is a possibility that the obtained result might be due to some sort of anticipatory effects caused by the protocols used. Therefore, the authors intend to compare the effects of ultrasound stimulation with placebo control in clinical conditions in a future study.

In this method, the measurement time of blood flow volume was 180 seconds, which seems insufficient to evaluate the effects of ultrasound acupuncture. However, a significant increase of blood flow volume was shown. Additional research should be done to establish whether the blood flow volume at 30 minutes after ultrasound stimulation changes in the same way or differently as compared with acupuncture stimulation.

Conclusions

The LR-3 acupoints were stimulated by focused ultrasound using a focused ultrasound device, and blood flow volume of the brachial artery was measured with an ultrasound system to evaluate the effect. Blood flow volume was increased significantly by both focused ultrasound stimulation and conventional acupuncture. Although a significant decrease of blood flow volume during acupuncture stimulation was observed, no such decrease was observed during ultrasound stimulation.

Disclosure Statement

No competing financial interests exist.

References

1. Hodgson JM, Reddy KG, Suneja R, et al. Intracoronary ultrasound imaging: Correlation of plaque morphology with angiography, clinical syndrome and procedural results in patients undergoing coronary angioplasty. J Am Coll Cardiol 1993;21:35–44.
2. Cusumano A, Coleman DJ, Silverman RH, et al. Three-dimensional ultrasound imaging: Clinical applications. Ophthalmology 1998;105:300–306.
3. Mitragotri S. Healing sound: The use of ultrasound in drug delivery and other therapeutic applications. Nat Rev Drug Discov 2005;4:255–260.
4. Robertson VJ, Baker KG. A review of therapeutic ultrasound: Effectiveness studies. Phys Ther 2001;81:1339–1350.
5. Yu T, Wang Z, Mason TJ. A review of research into the uses of low level ultrasound in cancer therapy. Ultrason Sonochem 2004;11:95–103.
6. ter Haar G. Therapeutic applications of ultrasound. Prog Biophys Mol Biol 2007;93:111–129.
7. ter Haar G. Therapeutic ultrasound. Eur J Ultrasound 1999; 9:3–9.
8. Tsuruoka N, Watanabe M, Seki T, et al. Acupoint stimulation device using focused ultrasound. Conf Proc IEEE Eng Med Biol Soc 2010;1258–1261.
9. Norheim AJ, Fonnebo V. Acupuncture adverse effects are more than occasional case reports: Results from questionnaires among 1135 randomly selected doctors, and 197 acupuncturists. Complement Ther Med 1996;4:8–13.
10. Ernst G, Strzyz H, Hagmeister H. Incidence of adverse effects during acupuncture therapy: A multicentre survey. Complement Ther Med 2003;11:93–97.
11. Takayama S, Seki T, Sugita N, et al. Radial artery hemodynamic changes related to acupuncture. Explore 2010;6: 100–105.
12. Takayama S, Seki T, Watanabe M, et al. Brief effects of acupuncture on the peripheral arterial system of the upper limb and systemic hemodynamics in humans. J Altern Complement Med 2010;16:707–713.
13. Baker KG, Robertson VJ, Duck FA. A review of therapeutic ultrasound: Biophysical effects. Phys Ther 2001;81:1351–1358.

Address correspondence to:
Noriko Tsuruoka, MS
Graduate School of Biomedical Engineering
Tohoku University
6-6-04 Aza-Aoba, Aramaki, Aoba-ku
Sendai 980-8579, Miyagi
Japan

E-mail: noriko.tsuruoka@bme.tohoku.ac.jp

Not Intended for Review or Reproduction
For Review Only
Not Intended for Distribution or Reproduction

OA1306-04

中空光ファイバを用いた光バイオプシーシステム

東北大学　松浦　祐司

1．はじめに

光による無侵襲な生体内組織診断である光バイオプシーは、生体組織の分子構造や化学組成を内視鏡下において分光法を用いて分析を行うものであり、悪性腫瘍の診断・早期発見や動脈硬化に伴う血管内壁の状態変化の診断等に応用可能な技術として注目されている。光バイオプシーに主に用いられる手法としては赤外分光法とラマン分光法が挙げられ、これらはそれぞれ検出メカニズムが異なる[1]ために分析対象により相補的に使用されることが多い。本稿では、ラマン分光と赤外分光の両方に適用可能な光プローブとして、細径かつ柔軟な中空光ファイバを用いることを提案し、各種の実証実験の結果を示す。また、これらの分光法を用いた診断において、二次元イメージを取得することが可能になれば、健常部と病変部の境界を特定することが可能となり、強力な診断ツールとなり得る。そこで、複数の中空光ファイバを束ねたバンドルファイバを用いて赤外スペクトラルイメージングを試行した結果についても述べる。また近年，腫瘍近傍の毛細血管や血管内プラークの検出法として注目されている光音響イメージングを光ファイバプローブを用いて行った結果についても併せて報告する。

2．ラマン分光システム

ラマン分光法においては通常、励起光と検出光は可視もしくは近赤外光であるために、石英系のガラス光ファイバをプローブとして使用することができる。しかし、石英ガラスから発生するラマン散乱光の影響を除去するために、励起光用ファイバの出射端にはファイバからのラマン散乱光を取り除くためのバンドパスフィルタが、また散乱光検出用ファイバの入射端には、励起光を除去するための低域通過フィルタが必要となり[2][3]、プローブ先端を細径化することは難しい。そこで我々のグループでは、ラマン散乱を生じない空気をコアとする中空光ファイバをラマン分光用プローブとして用いることを提案した[4]。

中空ファイバは通常の光ファイバとは異なり、屈折率の低い空気や不活性ガスなどをコアとし、高屈折率の誘電体もしくは損失性の金属でクラッディングを構成したものである[5][6]。しかし、中空ファイバのコア・クラッド境界では全反射が生じないため、光は損失を伴いながらファイバ内を伝搬するが、ファイバ内面における反射率を高めて１に近づけることができれば、低損失伝送が実現可能となる。その方法として我々のグループでは、平滑な表面をもつ溶融石英ガラスキャピラリチューブを母材とし、その内面に目的とする波長において高反射率を示す金属薄膜を形成し、さらにその表面に誘電体薄膜による高反射コーティングを施すことにより低損失な中空ファイバを構成している[7]。

中空光ファイバはラマンノイズを発生しないため、その先端にフィルタを取り付ける必要がないうえ、励起光と検出光の両方を単一のファイバで伝送することが可能なため、プローブの細径化が容易である。図１は中空光ファイバプローブを用いたラマン分光測定系の概要である。プローブとしては、ガラスキャピラリの内面に銀薄膜を形成した中空光ファイバ（内径700 μm、長さ1.5 m）を用い、その先端にはボールレンズが取り付けられている。励起光源としては波長785 nmのチタンサファイアレーザを用い、単レンズにより中空光ファイバへ結合している。検出した光は低域通過フィルタとノッチフィルタでストークス光のみを得て、冷却CCDを用いたラマン分光器によりスペクトルを測定する。

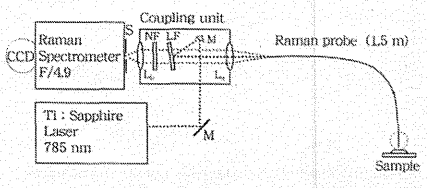

図１　中空光ファイバプローブを用いたラマン分光測定系

この測定系を用いてラット胃のスペクトルをインビボで測定することを試みた。測定では直径2 mmの細径内視鏡を用い、測定の前にはラマンスペクトル測定の支障となる蛍光を発生する残渣などを除去するため、胃を洗浄した。図２は測定したラット胃のスペクトルであり、左が得られた生のスペクトル、右は蛍光バックグラウンドを除去した後のスペクトルである。数値的な処理によりバックグランドノイズを除去することにより、タンパク質中のアミドや炭水化物などの明確なラマン散乱ピークが得られた。

3．赤外分光システム

フーリエ変換赤外分光光度計（FTIR）を用いた赤外吸収分光も生体組織の分析に有効である。これまでに、カルコゲナイドガラスファイバや多結晶ファイバが赤外光用伝送路として開発されているが[8][9]、材料の毒性や化学的耐久性に問題があり、医療への適用が難しい。そこで我々は中空光ファイバをリモート赤外分光用プローブとして用いることを提案した[10]。

中空光ファイバプローブを用いた赤外分光測定系の概要を図３に示す。FTIR内部のグローバ光源からの光は、金被膜軸外しミラーにより集光され、中空光ファイバ（長さ50 cm、内径2 mm）へと入射する。ファイバの先端には図中に示すような構造のシリコン製減衰全反射（ATR）プリズムが取り付けられている。プリズムに入射した光はプリズムの斜面で２回全反射されファイバへ戻るが、全反射する際にプリズムが接している測定対象物に光の一部のパワーが結合するため、測定対象物の吸収特性を測定することが可能である。

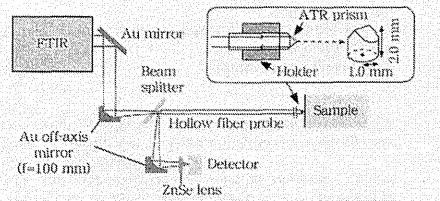

図３　中空光ファイバプローブを用いた赤外分光測定系

本測定系を用いた非侵襲血液成分測定システムについて検討した。血糖値測定に一般的に用いられている近赤外分光では、分子振動の倍音・結合音を検出するのに対し、赤外分光は基本振動を検出するため、高感度かつ高精度な分析が可能である。なお、測定対象は、毛細血管へのアプローチが容易な口腔粘膜とした。図

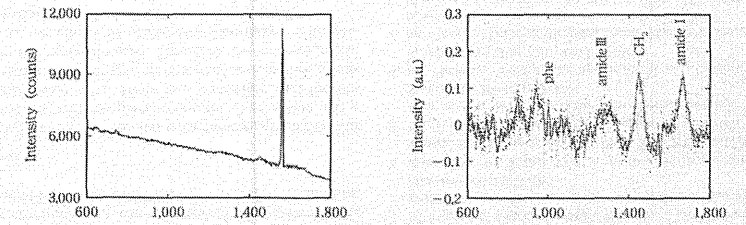

(a) 処理前　　(b) バックグラウンド差分後

図２　インビボで測定したラット胃内壁のラマンスペクトル

0917-026X/13/¥503/論文/JCOPY

4に健常者の口腔粘膜の赤外吸収スペクトルを示す。1,040 cm^{-1}付近にグルコースの吸収、3,300 cm^{-1}と1,620 cm^{-1}にそれぞれ水のOH伸縮振動吸収、変角振動吸収に起因する明瞭なピークが確認された。図5は採血により測定したグルコース濃度と本測定系で測定した結果の相関である。プリズムの押しつけ圧力の変動などによる影響を低減するため、OH伸縮振動および変角振動吸収ピークを基準として、グルコースの吸収ピークとの吸光度比を算出している。高い水分濃度を示す口腔粘膜の測定では、OHの吸収ピークを基準として用いることが可能であると思われる。

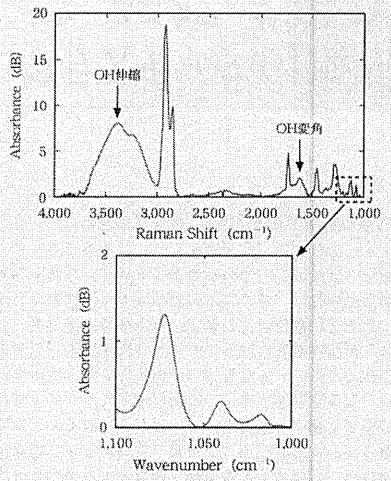

図4　健常者の口腔粘膜の赤外吸収スペクトル

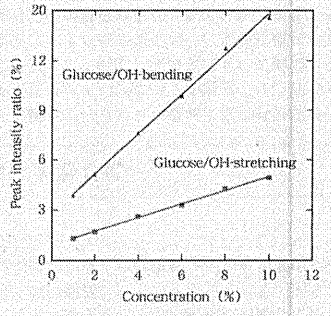

図5　採血により測定したグルコース濃度と本測定系で測定した結果の相関

4．中空光ファイババンドルによる分光スペクトラルイメージング

二次元平面において、前項で述べた分光スペクトルを取得して得られる分光イメージを用いることにより、平面内における特定分子の分布状況などを知ることが可能となる。さらに内視鏡下での分光イメージングができれば、内臓や血管といった体内組織表面における病変部と健常部の境界づけが可能となり、光バイオプシーの強力なツールとなる。二次元のイメージングを行うためには、内視鏡に何らかの機構を組み込み、ファイバ先端部をスキャンする手法と、複数のファイバをコヒーレントに束ねたバンドルファイバを用いる手法が考えられる。本稿では後者を採用することとし、中空光ファイバを用いたバンドルファイバを試作しその評価を行った。

スペクトラルイメージング取得のための実験では、赤外イメージ伝送用バンドルファイバとして内径320 μm、長さ45 cmの中空光ファイバを19本六方格子状に束ねたものを用いた。このバンドルの最小曲げ半径は35 mm程度である。FTIRからの光を中空ファイバプローブに入射させ、その出射端にサンプルを配置することにより、その透過光イメージングを高速度赤外カメラ（InSb素子）によって撮像した。カメラで観測した各ピクセルにおけるインターフェログラムをフーリエ変換することにより、サンプルの赤外透過スペクトラルイメージングを行った。

厚さ40 μmの畜肉（ブタ）片を二枚のカバーガラス（厚さ150 μm）に挟んで、プローブの中央部分に赤味と脂肪分の境界が配置された状態でイメージングを行った。図6は各ピクセルにおいて、コレステロールの吸収ピーク波長に相当する3.4 μmから3.7 μmにおける透過スペクトルの積分値をマッピングしたものであり、フィルタリング関数を利用してスムージング処理されている。両領域の境界部分が検出されており、本システムが赤外スペクトラルイメージングシステムとして機能することが示された。

5．中空光ファイババンドルを用いた光音響イメージング

光音響イメージングは、従来のモダリティでは観察できなかった深部の新生血管などを高分解能にイメージングできることが期待されている。我々のグループでは、内視鏡下へ適用可能な小型かつ高感度な光ファイバ超音波プローブを開発し、本プローブと中空光ファイババンドルを組み合わせることでセンサ部におけるスキャン機構を必要としないイメージングプローブについて検討した。

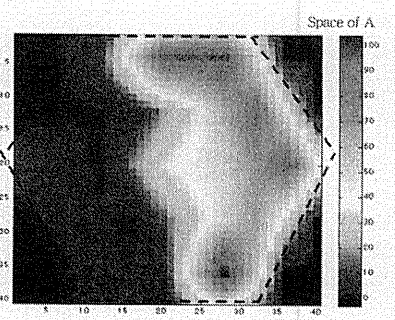

図6　コレステロール吸収ピーク波長におけるブタ肉片の透過光スペクトラルイメージ
試料左半分に脂肪部が存在している。

図7に光ファイバプローブの構成を示す。DFBレーザ（波長1.550 nm）から出射されたレーザ光は光ファイバサーキュレータによりセンサ部へと伝送される。センサ部にはファイバ先端にファブリペロー干渉計として機能するポリマー薄膜が形成されており、超音波による音圧が弾性的なポリマー膜に与える光路差の変化が出力光の強度変化として検出される。なお、本システムでは光通信用として市販されている光コンポーネントを使用しているため、高感度かつ安定性に優れた干渉計を低コストで構築できることが利点の1つである。

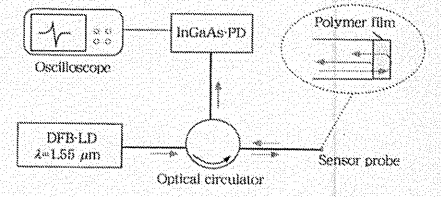

図7　光音響検出用光ファイバプローブの構成

図8に本プローブを用いて構成可能なイメージングシステムの概要を示す。単一のプローブを励起光伝送用の中空光ファイババンドルの中央に配置する。バンドルの入射端はアレイ状になっているためレーザ光を入射端で走査することによりイメージ取得が可能である。この構成を用いれば先端部に走査機構をもたない細径なイメージングシステムを構築可能である。中空光ファイバは光音響測定に用いられるピークパワーの大きいナノ秒光パルスを低損失に伝送可能であり、さらに実効的なNAが0.05程度ときわめて小さいため、ほぼ平行な出射光が得られることから、ファイバ先端にレンズを配置する必要がないという2つの利点をもっている。

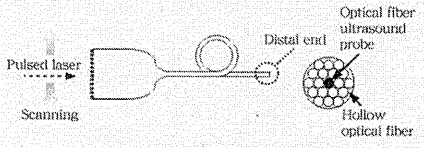

図8　光音響イメージング用光ファイバプローブの構成

本システムの実現可能性を検証するため、内径320 μmの中空光ファイバ4本をアレイ状に配置したシステムを用いてイメージ取得を試みた。励起光源にはQスイッチNd:YAGレーザの第2高調波（波長532 nm）を使用し、パルスエネルギー0.7 mJのレーザ光をファイバ入射端側でスキャンすることでファイバ素子毎にサンプルに照射した。なおサンプルには黒色吸

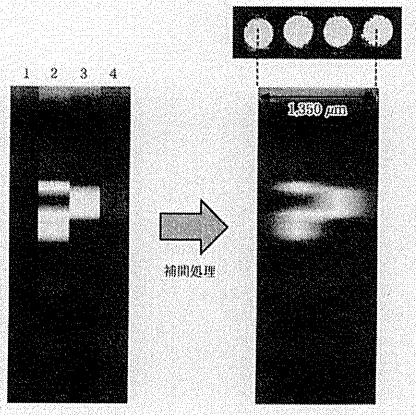

図9　アレイ状プローブを用いて観測したチューブ状サンプルの光音響イメージ

収体を満たした1 mmのシリコンチューブを使用した。図９左は４素子それぞれの励起に対応して得られた各信号を輝度変換したものを示しており、図９右のように補間処理を施した結果サンプルを可視化することに成功した。

6．おわりに

内視鏡下でのラマン分光および赤外分光を行うための中空光ファイバプローブを提案した。赤外分光用のプローブとして幅広い波長域において低損失性を示す中空光ファイバが有効であり、生体組織の測定に十分な信号強度が得られることを示した。また、ラマン分光においては先端にボールレンズを取り付けた中空光ファイバをプローブとして用い、細径内視鏡との組み合わせによりインビボでの光バイオプシーへの対応が可能なことを示した。さらに、中空光ファイバを用いたイメージバンドルファイバを試作し、赤外スペクトラルイメージングが可能なことを示すとともに、バンドル中空ファイバを用いた光音響イメージング取得も試みた。現状ではバンドルの直径は数mm程度と大きく、また素子数も小さいためにその用途は限定されるが、今後はファイバの細径化により、内視鏡下での利用な可能なバンドルの作製を行い、これを用いて各種イメージングを行うことを試みる。これらのファイバプローブは柔軟かつ無毒、また耐久性にも優れるため、生体内部での使用に適したものであり、今後もさまざまなアプリケーションへの応用展開が期待される。

〈参考文献〉

(1) 南茂夫・合志陽一　編：分光技術ハンドブック（朝倉書店、1990）
(2) T. F. Cooney, C. L. Schoen, S. K. Sharma and D. M. Carey：Appl. Spectroscopy 47, 1683 (1993)
(3) Y. Komachi, H. Sato, K. Aizawa and H. Tashiro：Appl. Opt. 44, 4722 (2005)
(4) Y. Komachi, H. Sato, Y. Matsuura, M. Miyagi and H. Tashiro：Opt. Lett. 30, 2942(2005)
(5) J. A. Harrington：*Infrared Fibers and Their Applications* (SPIE press, Bellingham, 2003)
(6) 宮城光信：光伝送の基礎、昭晃堂（1991）
(7) Y. Abe, Y. Matsuura, Y. Shi, Y. Wang, H. Uyama and M. Miyagi：Opt. Lett. 23, 89 (1998)
(8) A. B. Seddon：J. *Non-Cryst. Solid* 184, 44 (1995)
(9) D. A. Pinnow, A. L. Gentile, A. G. Standlee, A. J. Timper and L. M. Hobrock：Appl. Phys. Lett. 33, 28 (1978)
(10) S. Kino, Y. Matsuura：Appl. Spectroscopy 61, 1334 (2007)

【筆者紹介】

松浦祐司

東北大学　大学院　医工学研究科計測・診断医工学講座
教授
〒980-8579　仙台市青葉区荒巻字青葉6-6-05
TEL：022-795-7108　FAX：022-795-7106
E-mail：yuji@ecei.tohoku.ac.jp

プラスチックの自動車部品への展開
―ケーススタディから読み解く現状と近未来―

ハイブリッド車や電気自動車といった次世代自動車の構成材料として期待されているプラスチックについて、研究者・技術者、ビジネスパーソン諸氏が、技術開発やビジネスの方向性を得られる一冊。

■主な内容
●次世代自動車の将来展望とプラスチックへの期待
●プラスチック製自動車部品を１４の分野に分け採用動向と展望を具体的に考察
●環境編では有害化学物質、車室内VOC、植物由来プラスチック、リサイクルについての現状と展望

日本工業出版㈱　0120-974-250
http://www.nikko-pb.co.jp/　netsale@nikko-pb.co.jp

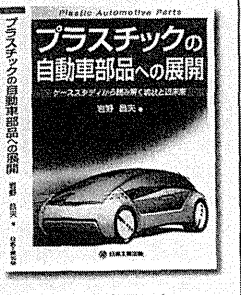

■著者：岩野昌夫
■体裁：A5版496頁
■定価：3,780円

DNA Research 20, 255–262, (2013)
Advance Access publication on 29 March 2013
doi:10.1093/dnares/dst007

Development and Characterization of cDNA Resources for the Common Marmoset: One of the Experimental Primate Models

Shoji Tatsumoto[1,†], Naoki Adati[1,‡], Yasushi Tohtoki[1,¶], Yoshiyuki Sakaki[1,§], Thorsten Boroviak[2], Sonoko Habu[3], Hideyuki Okano[4], Hiroshi Suemizu[5], Erika Sasaki[6], and Masanobu Satake[7,*]

RIKEN Genomic Sciences Center, Suehiro-cho 1-7-22, Tsurumi-ku, Yokohama 230-0045, Japan[1]; Centre for Stem Cell Research, Wellcome Trust and Medical Research Council Stem Cell Institute, University of Cambridge, Tennis Court Road, Cambridge CB2 1QR, UK[2]; Department of Immunology, Juntendo University School of Medicine, Hongo 2-1-1, Bunkyo-ku, Tokyo 113-8421, Japan[3]; Department of Physiology, School of Medicine, Keio University, Shinano-machi 35, Shinjyuku-ku, Tokyo 160-8582, Japan[4]; Biomedical Research Department, Central Institute for Experimental Animals, Tonomachi 3-25-12, Kawasaki-ku, Kawasaki 210-0821, Japan[5]; Department of Applied Developmental Biology, Central Institute for Experimental Animals, Tonomachi 3-25-12, Kawasaki-ku, Kawasaki 210-0821, Japan[6] and Institute of Development, Aging and Cancer, Tohoku University, Seiryo-machi 4-1, Aoba-ku, Sendai 980-8575, Japan[7]

*To whom correspondence should be addressed. Tel. +81-22-717-8477. Fax. +81-22-717-8482.
Email: satake@idac.tohoku.ac.jp

Edited by Dr Toshihiko Shiroishi
(Received 9 May 2012; accepted 1 March 2013)

Abstract

The common marmoset is a new world monkey, which has become a valuable experimental animal for biomedical research. This study developed cDNA libraries for the common marmoset from five different tissues. A total of 290 426 high-quality EST sequences were obtained, where 251 587 sequences (86.5%) had homology ($1E^{-100}$) with the Refseqs of six different primate species, including human and marmoset. In parallel, 270 673 sequences (93.2%) were aligned to the human genome. When 247 090 sequences were assembled into 17 232 contigs, most of the sequences (218 857 or 15 089 contigs) were located in exonic regions, indicating that these genes are expressed in human and marmoset. The other 5578 sequences (or 808 contigs) mapping to the human genome were not located in exonic regions, suggesting that they are not expressed in human. Furthermore, a different set of 118 potential coding sequences were not similar to any Refseqs in any species, and, thus, may represent unknown genes. The cDNA libraries developed in this study are available through RIKEN Bio Resource Center. A Web server for the marmoset cDNAs is available at http://marmoset.nig.ac.jp/index.html, where each marmoset EST sequence has been annotated by reference to the human genome. These new libraries will be a useful genetic resource to facilitate research in the common marmoset.

Key words: *common marmoset; cDNA; gene resource*

1. Introduction

The mouse is a widely used and well-studied model animal for biomedical research. Many techniques for sophisticated genetic manipulations to model diseases have been established and researchers hope that the results obtained can be extrapolated to humans. Although this assumption is true in some cases, there are several areas of biomedical research where this proves to be more difficult. These areas include neuroscience, behavioural research, toxicology, drug development, and infectious diseases.[1] To overcome these limitations, efforts have been made to carry out biomedical studies in non-human primate model organisms, as the latter are more closely related to humans.

One of these established non-human primate model organisms is *Callithrix jacchus* (common marmoset). The marmoset is a small new world monkey and offers many advantages as an experimental animal over other non-human primates. It is small in size, which makes it comparatively easy to handle. Furthermore, it has been bred in captivity and its progeny have been maintained for >30 years in laboratory environments. Also, it does not harbour or transmit hazardous infectious agents. Therefore, the common marmoset is increasingly used in biomedical research worldwide. For example, models of autoimmune diseases involving the central nervous system have been developed in the common marmoset and it has been used extensively as a primate model.[2–4] More recently, genetically modified common marmosets have been produced successfully and their transgenes have been transmitted through the germ line.[5] In the future, it would be very useful to develop transgenic marmosets as models of human diseases.

Intensive efforts have been made to develop research tools for using the common marmoset as an experimental animal. For instance, several lines of monoclonal antibodies have been prepared, which are directed against immunity-related antigens of the marmoset.[6–8] Many, but not all anti-human antigen antibodies cross-reacted with the corresponding marmoset antigens, so it was necessary to establish marmoset-specific antibodies.[9] A pilot gene analysis study reported cDNA sequencing of immunity-related genes.[10] Based on genome-wide analyses, a draft sequence of the common marmoset, known as caljac3, was produced and made available to the public via the genome browser of the University of California Santa Cruz (http://genome.ucsc.edu/).

The current study describes the preparation of cDNA libraries for the common marmoset using five different cell types/tissues, which resulted in the identification of 290 426 high-quality EST sequences. These sequences were characterized by comparison with the sequences of six primate species, including humans. Overall, the EST sequences transcribed in the marmoset shared many common features with those from humans, whereas a small fraction was found to be unique to the marmoset.

2. Materials and methods

2.1. RNA extraction and library construction

Cytoplasmic RNA was extracted from the liver (MLI), brain and spinal cord (MSC), spleen (MSP), testis (MTE), and embryonic stem (ES) cells (MES) of the common marmoset using Trizol reagent. Marmoset ES cells were cultured as described previously.[11] Full-length cDNA libraries were constructed from the total RNAs of the aforementioned tissues/cells using a vector-capping method.[12] cDNAs generated from MLI, MSC, MSP, MTE, and MES were ligated into pGCAP1, pGCAPzf3, pGCAPzf3, pGCAP10, and pGCAP10 vectors, respectively. Colonies of *Escherichia coli* transformants were picked randomly, inoculated into 384-well plates using a Flexys colony picker (Genomic Solutions Ltd., Cambridgeshire, UK), and stored at −80°C.

2.2. EST sequencing

Colonies were picked from 99 plates for MSC; 200 plates each for MES, MSP, and MTE; and 201 plates for MLI (Supplementary Table S1). Sequencing templates were prepared using a TempliPhi DNA Amplification Kit (GE Healthcare UK Ltd., Buckinghamshire, UK). The sequencing reactions for the 5′-end directional ESTs were conducted using a BigDye Terminator v3.1 Cycle Sequencing Kit (Applied Biosystems, Inc., CA, USA). The sequence primers used for pGCAP1, pGCAP10, and pGCAPzf3 were 5′-AGGCCTGTACGGAAGTGT-3′, 5′-AGGCCTGTACGGAAGTGT-3′, and 5′-CAAGGCGATTAAGTTGGGT-3′, respectively. The sequencing reaction products were purified by ethanol precipitation and loaded onto 3730 DNA Analyzers (Applied Biosystems Inc.).

2.3. Selection of high-quality EST data

The raw sequence data were basecalled using the KB basecaller program, which identified 345 600 sequences. A cross-match program was applied to the raw data to remove sequences derived from vectors and those added as caps during plasmid construction (−minimach 10, −minscore 20). Low-quality sequences [quality value (QV) = one for each nucleotide ± 3 neighbouring nucleotides measuring <105 in length] were masked by *N* (average QV > 15). If *N* was longer than 10 nucleotides, sequences located 3′ of these *N* were removed. Finally, only high-quality sequences longer than 100 nucleotides were selected and used in further analyses (see the high quality column, Supplementary Table S1). There were 290 426 high-quality ESTs, which represented 84% of the raw sequence data. High-quality EST sequences were obtained frequently and were relatively abundant (93%) in MES and

† Present address: National Institute of Genetics, Yata 1111, Mishima 411-8540, Japan.
‡ Present address: Research Equipment Center, Hamamatsu University School of Medicine, Handayama 1-20-1, Higashi-ku, Hamamatsu 431-3192, Japan.
¶ Present address: Division of Cancer Genomics, National Cancer Center Research Institute, Tsukiji 5-1-1, Chuo-ku, Tokyo 104-0045, Japan.
§ Present address: Toyohashi University of Technology, Hibarigaoka 1-1, Tenpaku-cho, Toyohashi 441-8580, Japan.

© The Author 2013. Published by Oxford University Press on behalf of Kazusa DNA Research Institute.
This is an Open Access article distributed under the terms of the Creative Commons Attribution License (http://creativecommons.org/licenses/by-nc/3.0/), which permits non-commercial use, distribution, and reproduction in any medium, provided the original work is properly cited. For commercial re-use, please contact journals.permissions@oup.com.

MTE, whereas their frequencies were comparatively low (72–80%) in MLI, MSC, and MSP.

The sequence length was higher in MES and MTE (702–706 nucleotides), than in MLI, MSC, and MSP (514–551 nucleotides; see the length column in Supplementary Table S1). The differences in the average length of readable sequences and the differences in the frequency of high-quality ESTs probably reflected the quality of each cDNA library. The cDNA libraries were also evaluated for transcription initiation sites by searching for the presence or absence of cap structure-derived guanine nucleotides at the extreme 5′ end of each EST (see the G-cap column, Supplementary Table S1). The frequency of G-cap-positive sequences was >80% in all five cDNA libraries, indicating that the synthesis of most cDNAs was initiated at the 5′ end.

2.4. *Registration of the sequences*

All of the EST sequences were deposited in the DNA Databank of Japan. Their accession numbers are as follows; HX373156 to HX444163 for MES cDNAs, HX444164 to HX500395 for MLI cDNAs, HX500396 to HX529651 for MSC cDNAs, HX529652 to HX591448 for MSP cDNAs, and HX591449 to HX663542 for MTE cDNAs.

2.5. *Tools used for sequence analyses*

The following tools were used for sequence analysis: BLAST (The Basic Local Alignment Search Tool) finds regions of local similarity between sequences. The program compares nucleotide or protein sequences to sequence databases and calculates the statistical significance of matches),[13] BLAT (The BLAST-Like Alignment Tool uses the index to find regions in the genome likely to be homologous to the query sequence),[14] CD-HIT (a widely used program for clustering and comparing protein or nucleotide sequences. CD-HIT helps to significantly reduce the computational and manual efforts in many sequence analysis tasks and aids in understanding the data structure and correct the bias within a dataset),[15] CAP3 (a DNA sequence assembly program),[16] cross_match (this tool uses cross_match to mask vector/adapter sequences and optimally trim vector sequence and/or polyA/T trail. It takes a set of sequences to be masked, and a set of vectors/adapters used to perform masking),[17] EMBOSS (getorf finds and extracts open reading frames),[18] and InterProScan (a protein domains identifier).[19]

3. Results and discussion

3.1. *EST clustering and assembly*

The 290 426 sequences obtained by normalization of ESTs as in Section 2.3 were clustered and/or assembled to estimate how many genes/transcriptional units were read as ESTs (Table 1). Overlapping sequences were clustered within the longest sequence using the CD-HIT program, whereas overlapping sequences were assembled and extended into a contig using the CAP3 program. According to the CD-HIT program, the number of clusters varied from 10 010 in MLI to 29 028 in MTE. The summed number of contigs and singletons ranged from 8831 in MLI to 25 909 in MTE. According to both programs, MTE had the highest number of clusters/assemblies, suggesting that the testis had the greatest number of expressed transcriptional units. Notably, there were some more clusters than assemblies in each cDNA library. In fact, the total and non-redundant numbers in the five different libraries were 62 210 clusters and 60 568 assemblies (Table 1). This small difference (62 210 versus 60 568) suggests that most of the EST sequences obtained correspond to the mRNA 5′ end (as for another indication of similar performance of CD-HIT and CAP3, see Supplementary Fig. S1).

3.2. *Assignment of marmoset ESTs to the Refseq mRNAs of primates*

All 290 426 sequences were examined by comparing them with the known sequences registered at the NCBI as Refseq mRNAs (http://ncbi.nlm.nih.gov/RefSeq/). Refseqs from six different primates were used in the reference dataset, including *Homo sapiens*, *Pan troglodytes*, *Pongo abelii*, *Macaca mulatta*, *Nomascus leucogenys*, and *C. jacchus*. It should be noted that the human Refseqs were based on cDNA sequences, whereas the Refseqs from other primate species were based mainly on the predictions of genomic sequences. The search program used was BLASTn and the threshold of significant homology was set to $1E^{-100}$, which was a very strict criterion.

Table 1. Clustering of ESTs by CD-HIT and assembly of ESTs by CAP3

Libraries	Number of ESTs	Number of clusters by CD-HIT	Number of contigs and singlets assembled by CAP3
MES	71 009	17 467	15 837 = 5519 (contig) + 10 318 (singlet)
MLI	56 232	10 010	8831 = 3319 (contig) + 5512 (singlet)
MSC	29 258	12 309	10 617 = 3764 (contig) + 6853 (singlet)
MSP	61 831	16 600	14 268 = 5086 (contig) + 9182 (singlet)
MTE	72 096	29 028	25 909 = 8044 (contig) + 17 865 (singlet)
All	290 426	62 210	60 568 = 17 232 (contig) + 43 336 (singlet)

Parameters used in CD-HIT and CAP3 programs were default.

A total of 239 920 and 231 084 sequences shared homology with human and marmoset Refseqs, respectively (Table 2). Homology with the combined Refseqs from the six primates was found for 251 587 sequences (85.6% of 290 426). Therefore, these 251 587 sequences were designated as primate homologues. The average length of the homologous sequences was 528 nucleotides. Of these 251 587 sequences, 4974 sequences were identical to their corresponding Refseq sequences, whereas 94 102 sequences shared 100% nucleotide sequence identity only with the aligned homologous regions. Additionally, 931 sequences shared homology with the Refseqs of non-primates. Most of these sequences were homologous to mouse Refseqs, suggesting that they were probably derived from mouse cells that were used as a feeder layer to culture ES cells.

Out of the above described 251 587 primate homologues, only sequences that shared homology with the Refseqs of all six primates were extracted, and that yielded 199 511 sequences. Then, for each of 199 511 sequences, the alignments between the EST and Refseq with the highest score among the six primates were selected, and 199 511 sequences were grouped into six for each primate species. Finally, the average identities and coverage were calculated using the alignments for each primate species (Table 3). As expected, the highest sequence identity (99%) was between the marmoset EST and marmoset Refseq. The average sequence identities between the marmoset EST and the Refseqs of the other five primate species were in a similar range (94–95%). Thus, the sequences differed by ~5% between the marmoset and the other five primates. The coverage was highest between the marmoset EST and human Refseq (91%), whereas it was lowest between the marmoset EST and marmoset Refseq (84%). This difference of 6% corresponded to 25 nucleotides, so it is likely that the alignment of the EST and marmoset Refseqs started 25 nucleotides downstream from the 5′ end of the marmoset Refseq. This might suggest that the 5′UTR of the marmoset Refseq was not predicted precisely from its genomic sequence.

In the above assignment of marmoset ESTs to primates' Refseqs in Table 2, the Refseqs used as references can be re-classified into non-overlapping, distinct gene entities. Homologous sequences of 239 920 and 231 084 corresponded to 13 825 human and 13 499 marmoset genes, respectively (see the numbers in parenthesis in Table 2). In addition, we searched for HomoloGenes (http://www.ncbi.nlm.nih.gov/homologene) that are found in common among *Homo sapiens*, *Pan troglodytes*, and *Macaca mulatta*, and detected 9879 Homologenes. When identities and coverage between marmoset ESTs and primates' Refseq were recalculated for these 9879 Homologenes (see the numbers in parenthesis in Table 3), coverage increased by 2–3%, whereas identity between marmoset and human remained the same (94–95%). Thus, it appears again plausible that the sequences diverge by 5% between marmoset and other primates including human.

Table 2. Assignment of common marmoset ESTs to primates' Refseq

Species derivation of Refseq	Number of ESTs homologous to Refseq (number of homologous genes)
Homo sapiens	239 920 (13 825)
Pan troglodytes	233 913 (14 372)
Callithrix jacchus	231 084 (13 499)
Pongo abelii	231 354 (13 898)
Macaca mulatta	229 151 (13 677)
Nomascus leucogenys	228 749 (13 296)
Six primates	251 587
Non-primates	931

EST sequences of common marmoset (total 290 426) were referred to primates' Refseq mRNA that are registered at NCBI. Homology was searched using BLASTn and judged significant at $<1E^{-100}$.

3.3. *Mapping marmoset ESTs to the human genome*

Each marmoset EST sequence (total 290 426 reads) was mapped to the human genome (hg19)

Table 3. Identity and coverage between homologous marmoset ESTs and primates' Refseq

Species derivation of Refseq	Identity for Refseq (for 9879 HomoloGenes)	Coverage for Refseq (for 9879 HomoloGenes)
Homo sapiens	94.88% (94.54%)	91.14% (93.91%)
Pan troglodytes	94.86% (94.54%)	88.84% (92.11%)
Callithrix jacchus	99.55%	84.70%
Pongo abelii	94.77%	87.36%
Macaca mulatta	94.73% (94.44%)	87.20% (89.66%)
Nomascus leucogenys	94.72%	87.80%

Identity (%) represents a degree of identity between the aligned two sequences of high-scoring segment pairs, whereas coverage (%) represents a ratio of aligned sequence length over an entire length of EST. See the text as for the details how identity and coverage were calculated.

using the BLAT search program. This showed that 99.1% of the ESTs (287 849 reads) mapped to the human genome (Table 4). This mapping result was filtered further using the UCSC Genome Browser and a pslCDnaFilter. Finally, 93.2% (270 673 reads) of the marmoset ESTs were assigned specifically and exactly to the human genome.

The nucleotide sequence identity between aligned sequences was calculated after each EST had been mapped to the genome (Supplementary Fig. S2). The majority of ESTs shared 90–96% identity with the human genome. The relatively low identity between the ESTs and human sequences was analogous to the identity between the EST and Refseq shown in Table 3. It should be noted that the degree of mapping to the human genome did not differ significantly among the five cDNA libraries (data not shown).

3.3.1. ESTs that were mapped to exonic regions of the human genome The CAP3 method identified 17 232 contigs (Table 1). The contig sequences represented those that were read multiple times in the overlapping regions and they were considered more reliable than single-read singletons. These 17 232 contigs were mapped onto the human genome according to the filtering method shown in Table 4. Furthermore, information from human Refseqs was used to determine whether the mapped contigs corresponded to exonic sequences of the human gene. This approach identified 15 089 contigs (88% of 17 232) that mapped onto the human genome and that corresponded to human Refseqs. These 15 089 contigs, which consisted of 218 857 ESTs, were considered to be representative of the genes that are commonly transcribed in marmosets and humans.

Of these 15 089 contigs, ESTs that were present in only one type of cDNA library were identified. Of these tissue-specific contigs, those with the highest numbers of constitutive ESTs are shown in Table 5. The contigs with >1000 ESTs were *ALB*, *HPR*, *ORM2*, and *ORM1* from MLI, and *PRM1* from MTE. Most of the genes listed in Table 5 are known to be characteristic of each specific cell type/tissue.

3.3.2. ES cell-specific transcripts Supplementary Table S2 shows previously reported cDNA/EST studies of primates other than the marmoset.[20–24] These species include *Pan troglodytes*, *Macaca fascicularis*, and *Chlorocebus sabaeus*, while the tissues included the brain, skin, liver, B lymphocytes, bone marrow, pancreas, spleen, thymus, and peripheral blood mononuclear cells. As the current study is the first example of the use of monkey-derived ES cells in EST studies, the ES-specific transcripts are mentioned briefly (see Supplementary Table S3 where the contigs containing >5 ESTs are listed).

The most notable were *LIN28A*, *NANOG*, and *SOX2* because, together with *OCT4*, they are known to reprogram human somatic cells to induced pluripotent stem cells.[25] *LIN28A* and *NANOG* contribute to the maintenance of pluripotency in stem cells.[26–28]

Table 4. Mapping of ESTs on the human genome

Libraries	Number of marmoset ESTs	Number of ESTs mapped on the human genome (raw data)	Number of ESTs mapped on the human genome (filtered)
MES	71 009	70 375	66 894 (94.2%)
MLI	56 232	55 602	52 405 (93.2%)
MSC	29 258	28 931	27 253 (93.1%)
MSP	61 831	61 300	58 170 (94.1%)
MTE	72 096	71 641	65 951 (91.5%)
All	290 426	287 849 (99.1%)	270 673 (93.2%)

Marmoset ESTs (290 426) were mapped on the human genome (hg19) by using a BLAT search program (−stepSize = 5, −minScore = 50, −minIdentity = 80, −repMatch = 2253). This initial mapping gave a number of 287 849 (99.1%) ESTs. These ESTs were then filtered, following a UCSC Genome Browser and using a pslCDnaFilter (−minId = 0.85, −minCover = 0.75, −globalNearBest = 0.0025, −minQSize = 20, −minNonRepSize = 16, −ignoreNs, −bestOveralp). Basis for adopting this filtering condition was as follows. A use of the condition such as (−minId = 0.95, −minCover = 0.25) selected only 159 309 ESTs (54.9%), indicating −minId = 0.95 to be extremely strict in the exactness. Therefore, we lowered the −minId to 0.85 (and −minCover = 0.25) and found the reasonably selected numbers of exact ESTs. Thus, under this −minId of 0.85, we then tried to improve the specificity by increasing −minCover to 0.75 (since 0.90 appeared too strict, 0.90 was not used). This −minCover number of 0.75 is roughly equal to the expected coverage of coding sequence [the average length of EST was 619 nt, and the average length of 5′UTR of human transcripts is 170 nt, therefore, an expected coverage between coding sequences and ESTs would be (619−170)/619 = 0.73]. Eventually, a condition of −minId = 0.85, −minCover = 0.75 filtered 270 673 ESTs (93.2%) as exact and specific.

Table 5. Top five genes expressed abundantly in each cDNA library

Libraries	Gene symbols	Descriptions	Number of ESTs
MES	*PYY*	Peptide YY	123
MES	*LIN28A*	Lin-28 homologue A	50
MES	*C6orf221*	Chromosome 6 open reading frame 221	46
MES	*NANOG*	Nanog homeobox	45
MES	*ERVMER34-1*	Endogenous retrovirus group MER34, member 1	28
MLI	*ALB*	Albumin	4492
MLI	*HPR*	Haptoglobin-related protein	1537
MLI	*ORM2*	Orosomucoid 2	1227
MLI	*ORM1*	Orosomucoid 1	1221
MLI	*APOA2*	Apolipoprotein A-II	673
MSC	*SNAP25*	Synaptosomal-associated protein, 25 kDa	109
MSC	*PLP1*	Proteolipid protein 1	58
MSC	*CALCA*	Calcitonin-related polypeptide alpha	51
MSC	*STMN2*	Stathmin-like 2	30
MSC	*THY1*	Thy-1 cell surface antigen	28
MSP	*MS4A1*	Membrane-spanning 4-domains, subfamily A, member 1	62
MSP	*ITGB2*	Integrin, beta 2	29
MSP	*HLA-DPA1*	Major histocompatibility complex, class II, DP alpha 1	26
MSP	*CLEC4F*	C-type lectin domain family 4, member F	20
MSP	*CD53*	CD53 molecule	18
MTE	*PRM1*	Protamine 1	1,198
MTE	*TNP1*	Transition protein 1	161
MTE	*HMGB4*	High mobility group box 4	139
MTE	*PHF7*	PHD finger protein 7	138
MTE	*DKKL1*	Dickkopf-like 1	107

Shown are the contigs that were detected only in one out of five cDNA libraries and possessed larger numbers of constituting ESTs.

C6orf221 (also known as *ECAT1*, ES cell-associated transcript 1) and *DPPA5* belong to the same gene family, and they are expressed specifically in human ES cells.[29,30] The frequent appearance of the claudin family (see *CLDN6*, *CLDN9*, *CLDN7*, and *CLDN4*) was also noted, although its biological significance is not known.

3.3.3. ESTs that were mapped onto the human genome outside exonic regions We noted that there was another category of contigs that was mapped onto the human genome, but not located in exonic regions (i.e. contigs that shared no homology with human Refseqs). These comprised 808 contigs (4.7% of 17 232) with 5578 ESTs. These 808 contigs represented transcribed genes in the marmoset. Although they were conserved in the human genome, they did not appear to be transcribed as genes; hence, they were not characterized as human genes.

Next, the number of marmoset cDNA libraries, in which each contig was expressed, was determined. The number of contigs with ESTs detected in libraries 1 (i.e. only MES), 2 (i.e. MES and MTE), 3, 4, and 5 (all of MES, MLI, MSC, MSP, and MTE) were 562, 195, 28, 7, and 6, respectively (808 in total). Of the 562 contigs, 29 were found in MES, 31 in MLI, 28 in MSC, 87 in MSP, and 387 in MTE (562 in total). It appeared that the genes expressed in the marmoset testes (387/562 = 69%) had an increased likelihood of not being expressed in humans compared with the genes expressed in other tissues (31%/4 = 7.8%).

Supplementary Table S4 shows the 20 contigs whose constituting ESTs' numbers were the largest among the 808 contigs. Interestingly, the five contigs that had the highest numbers of ESTs (ID: 198, 15591, 1258, 1567, and 3721) also had ESTs in all five libraries. In the previous paragraph, it was noted that six contigs were expressed in all five libraries. It was found that five out of these six contigs were widely expressed at a high level in the marmoset. This suggests that actively expressed genes in the marmoset may even be non-transcribed as genes in humans. Many of the remaining genes in Supplementary Table S4 were expressed in a combination of tissues e.g. MLI and MSP, or MLI and MSC, or only in MTE.

3.3.4. Characterization of 808 contigs in non-coding RNA or silent regions of the human genome The 808 contigs described above were mapped onto the human genome, but did not have any corresponding human Refseqs. The human genome browser at UCSC also supports mapping of RNA-seq and large intergenic non-coding RNAs (linc RNA).[31,32] The locations of these RNA-seq/linc RNAs were checked in relation to the marmoset ESTs mapped onto the human genome. The tissues that are used in common in RNA-seq/linc RNA studies[31,32] and the current study are the liver, brain, and testis; hence, 138 contigs expressed in MLI, 125 in MSC, and 516 in MTE (total 779) were used for the analyses (Supplementary Table S5). This showed that 500 contigs (64% of 779) matched RNA-seqs, while 98 contigs had corresponding sequences in RNA-seq and linc RNA. However, 259 contigs (33% of 779) did not have any counterparts in RNA-seq or linc RNA, suggesting that they were not expressed as RNA.

In summary, of the 808 contigs that did not have a corresponding human Refseq, two-thirds were probably expressed as non-coding RNA, whereas the other third appeared to be silent. This potentially suggests that these 808 may have lost their characteristics as genes during human evolution.

3.3.5. Identification of so far unknown genes based on probable full-length cDNA sequences The degree of conservation and/or divergence in marmoset and human genes was analysed using the following approach as well. Supplementary Fig. S3A shows a flow chart of the method used for selecting 'unknown genes.' First, getorf in EMBOSS was applied to extract 60 568 unigenes (see Table 1 where 60 568 represents the sum of contigs and singlets). Thus, sequences were selected that contain an open-reading frame spanning an initiating methionine through to a stop codon, with a poly(A) tail at the 3′ end. The G-cap was preserved in most ESTs, so the selected sequences probably represented 'full-length' cDNAs. This approach selected 3151 unigenes.

Each unigene was mapped onto the human genome. In total, 2595 sequences were mapped onto the human genome. Of the 556 marmoset sequences that could not be mapped onto the human genome, 127 were annotated and identified using the Refseq information of all living species, while 311 (306 + 5) shared homology with sequences registered in EST/nr sequence databases. The remaining 118 unigenes could not be annotated, suggesting that they represent potentially unknown genes.

Notably, only 1 sequence was derived from MLI and MSC, 3 from MSP, 14 from MES, while 104 from MTE. This might indicate comparatively abundant expression of unknown genes in the marmoset testis. The length of the polypeptides encoded by the 'unknown genes' ranged from 11 to 131 amino acids, with an average of 47 (Supplementary Fig. S4). It should be noted that no known domains/motifs were detected in these 'unknown' amino acid sequences using the INTERPRO program.

3.3.6. Further characterization of the 118 'unknown genes' It is possible that the 118 genes with ORFs might not encode polypeptides but may represent non-coding RNAs. In fact, five shared homology (1e-5) with non-coding RNAs in a comprehensive database (http://www.ncrna.org/frnadb/) and a marmoset-derived non-coding RNA database (ftp://ftp.ensembl.org/pub/release 70/fasta/callithrix_jacchus/ncrna/). Furthermore, 66 out of 118 genes could be aligned with the human genome if a 75% sequence similarity was employed, and each of these alignments covered more than half of each sequence. Therefore, a significant portion of the 118 genes had features of both polypeptide-coding genes and non-coding RNAs. Supplementary Fig. S3B and its legend provide further details on the unbiased approach used to identify unknown genes.

3.4. Availability of the resources

A Web server of marmoset cDNAs has been constructed (http://marmoset.nig.ac.jp/index.html), in which each marmoset EST sequence is mapped onto the human genome. Information accessible via the human genome browser can be obtained on this server, including the Ensembl gene annotation, Refseqs, and RNA-seq/linc RNA. This Web server can be used as a search engine, so the marmoset EST sequences can be BLASTed and the results displayed. The cDNAs libraries and/or the clones are available upon request from the DNA Bank, RIKEN BioResource Center (RDB no. 6388–6392). These deposited resources are expected to be valuable for future studies that use the common marmoset as an experimental animal model.

Acknowledgements: S.T. and M.S. are very grateful to Atsushi Toyoda (National Institute of Genetics, Mishima, Japan) for his continuous encouragement, which helped us to accomplish this work. We thank members of Sequence Technology Team, RIKEN Genomic Sciences Center for the generation of marmoset ESTs.

Supplementary data: Supplementary Data are available at www.dnaresearch.oxfordjournals.org.

Funding

Sequencing work was supported by a Special Fund for RIKEN Genomic Sciences Center.

References

1. Mansfield, K. 2003, Marmoset models commonly used in biomedical research, *Comp. Med.*, **53**, 383–92.
2. Massacesi, L., Genain, C., Lee-Parritz, D., et al. 1995, Active and passively induced experimental autoimmune encephalomyelitis in common marmosets: a new model for multiple sclerosis, *Ann. Neurol.*, **37**, 519–30.
3. Genain, C. and Hauser, S. 2001, Experimental allergic encephalomyelitis in the new world monkey Callithrix jacchus, *Immunol. Rev.*, **183**, 159–92.
4. 't Hart, B., Laman, J., Bauer, J., et al. 2004, Modeling of multiple sclerosis: lessons learned in a non-human primate, *Lancet Neurol.*, **3**, 588–97.

5. Sasaki, E., Suemizu, H., Shimada, A., et al. 2009, Generation of transgenic nonhuman primates with germline transmission, *Nature*, **459**, 515–6.
6. Izawa, K., Tani, K., Nakazaki, Y., et al. 2004, Hematopoietic activity of common marmoset CD34 cells isolated by a novel monoclonal antibody MA24, *Exp. Hematol.*, **32**, 843–51.
7. Ito, R., Maekawa, S., Kawai, K., et al. 2008, Novel monoclonal antibodies recognizing different subsets of lymphocytes from the common marmoset (Callithrix jacchus), *Immunol. Lett.*, **121**, 116–22.
8. Kametani, Y., Suzuki, D., Kohu, K., et al. 2009, Development of monoclonal antibodies for analyzing immune and hematopoietic systems of common marmoset, *Exp. Hematol.*, **37**, 1318–29.
9. Brok, H., Hornby, R., Griffiths, G., et al. 2001, An extensive monoclonal antibody panel for the phenotyping of leukocyte subsets in the common marmoset and the cotton-top tamarin, *Cytometry*, **45**, 294–303.
10. Kohu, K., Yamabe, E., Matsuzawa, A., et al. 2008, Comparison of 30 immunity-related genes from the common marmoset with orthologues from human and mouse, *Tohoku J. Exp. Med.*, **215**, 167–80.
11. Sasaki, E., Hanazawa, K., Kurita, R., et al. 2005, Establishment of novel embryonic stem cell lines derived from the common marmoset (*Callithrix jacchus*), *Stem Cells*, **23**, 1304–13.
12. Ohtake, H., Ohtoko, K., Ishimaru, Y., and Kato, S. 2004, Determination of the capped site sequence of mRNA based on the detection of cap-dependent nucleotide addition using an anchor ligation method, *DNA Res.*, **11**, 305–9.
13. Altschul, S.F., Gish, W., Miller, W., et al. 1990, Basic local alignment search tool, *J. Mol. Biol.*, **215**, 403–10.
14. Kent, W.J. 2002, BLAT—the BLAST-like alignment tool, *Genome Res.*, **12**, 656–64.
15. Li, W. and Godzik, A. 2006, Cd-hit: a fast program for clustering and comparing large sets of protein or nucleotide sequences, *Bioinformatics*, **22**, 1658–9.
16. Huang, X. and Madan, A. 1999, CAP3: a DNA sequence assembly program, *Genome. Res.*, **9**, 868–77.
17. Ewing, B. and Green, P. 1998, Base-calling of automated sequencer traces using phred. II. Error probabilities, *Genome. Res.*, **8**, 186–94.
18. Rice, P., Longden, I. and Bleasby, A. 2000, EMBOSS: the European Molecular Biology Open Software Suite, *Trends in Genet.*, **16**, 276–7.
19. Quevillon, E., Silventoinen, V., Pillai, S., et al. 2005, InterProScan: protein domains identifier, *Nucleic Acids Res.*, **33**, 116–20.
20. Sakate, R., Osada, N., Hida, M., et al. 2003, Analysis of 5′-end sequences of chimpanzee cDNAs, *Genome. Res.*, **13**, 1022–6.
21. Chen, W.H., Wang, X.X., Lin, W., et al. 2006, Analysis of 10,000 ESTs from lymphocytes of the cynomolgus monkey to improve our understanding of its immune system, *BMC Genomics*, **7**, 82.
22. Uno, Y., Suzuki, Y., Wakaguri, H., et al. 2008, Expressed sequence tags from cynomolgus monkey (*Macaca fascicularis*) liver: a systematic identification of drug-metabolizing enzymes, *FEBS Lett.*, **582**, 351–8.
23. Osada, N., Hirata, M., Tanuma, R., et al. 2009, Collection of *Macaca fascicularis* cDNAs derived from bone marrow, kidney, liver, pancreas, spleen, and thymus. *BMC Res. Notes*, **2**, 199.
24. Tchitchek, N., Jacquelin, B., Winker, P., et al. 2012, Expression sequence tag library derived from peripheral blood mononuclear cells of the chlorocebus sabaeus, *BMC Genomics*, **13**, 279.
25. Yu, J., Vodyanik, M.A., Smuga-Otto, K., et al. 2007, Induced pluripotent stem cell lines derived from human somatic cells, *Science*, **318**, 1917–20.
26. Mitsui, K., Tokuzawa, Y., Itoh, H., et al. 2003, The homeoprotein Nanog is required for maintenance of pluripotency in mouse epiblast and ES cells, *Cell*, **113**, 631–42.
27. Darr, H. and Benvenisty, N. 2009, Genetic analysis of the role of the reprogramming gene *LIN-28* in human embryonic stem cells, *Stem Cells*, **27**, 352–62.
28. Xu, B., Zhang, K. and Huang, Y. 2009, Lin28 modulates cell growth and associates with a subset of cell cycle regulator mRNAs in mouse embryonic stem cells, *RNA*, **15**, 357–61.
29. Kim, S.K., Suh, M.R., Yoon, H.S., et al. 2005, Identification of developmental pluripotency associated 5 expression in human pluripotent stem cells, *Stem Cells*, **23**, 458–62.
30. Pierre, A., Gautier, M., Callebaut, I., et al. 2007, Atypical structure and phylogenomic evolution of the new eutherian oocyte- and embryo-expressed *KHDC1/DPPA5/ECAT1/OOEP* gene family, *Genomics*, **90**, 583–94.
31. Wang, E.T., Sandberg, R., Luo, S., et al. 2008, Alternative isoform regulation in human tissue transcriptomes, *Nature*, **456**, 470–6.
32. Cabili, M.N., Trapnell, C., Goff, L., et al. 2011, Integrative annotation of human large intergenic noncoding RNAs reveals global properties and specific subclasses, *Genes Dev.*, **25**, 1915–27.